Exploring the Influence of Lateral Conductivity Contrasts on the Storm Time Behavior of the Ground Electric Field in the Eastern United States

Elena Marshalko[1,2,3], **Mikhail Kruglyakov**[1,4], **Alexey Kuvshinov**[1], **Benjamin S. Murphy**[5], **Lutz Rastätter**[6], **Chigomezyo Ngwira**[6,7], and **Antti Pulkkinen**[6]

[1]Institute of Geophysics, ETH Zürich, Zürich, Switzerland, [2]Institute of Physics of the Earth, Moscow, Russia, [3]Geophysical Center, Moscow, Russia, [4]Geoelectromagnetic Research Center, Institute of Physics of the Earth, Moscow, Russia, [5]College of Earth, Ocean, and Atmospheric Sciences, Oregon State University, Corvallis, OR, USA, [6]NASA Goddard Space Flight Center, Greenbelt, MD, USA, [7]Department of Physics, The Catholic University of America, Washington, DC, USA

Abstract The intensification of the fluctuating geomagnetic field during space weather events leads to generation of a strong electric field in the conducting earth, which drives geomagnetically induced currents (GICs) in grounded technological systems. GICs can severely affect the functioning of such infrastructure. The ability to realistically model the ground electric field (GEF) is important for understanding the space weather impact on technological systems. We present the results of three-dimensional (3-D) modeling of the GEF for the eastern United States during a geomagnetic storm of March 2015. The external source responsible for the storm is constructed using a 3-D magnetohydrodynamic (MHD) simulation of near-Earth space. We explore effects from conductivity contrasts for various conductivity models of the region, including a 3-D model obtained from inversion of EarthScope magnetotelluric data. As expected, the GEF in the region is subject to a strong coastal effect. Remarkably, effects from landmass conductivity inhomogeneities are comparable to the coastal effect. These inhomogeneities significantly affect the integrated GEF. This result is of special importance since the computation of GICs relies on integrals of the GEF (voltages), but not on the GEF itself. Finally, we compare the GEF induced by a laterally varying (MHD) source with that calculated using the plane wave approximation and show that the difference is perceptible even in the regions that are commonly considered to be negligibly affected by lateral nonuniformity of the source. Overall, the difference increases toward the north of the model where effects from laterally variable high-latitude external currents become substantial.

1. Introduction

During the last decade many studies aimed at three-dimensional (3-D) computations of the ground (surface) electric field (GEF) in different regions of the world during space weather events have been conducted. The papers on the topic can be divided into three major groups. Computations of the GEF within the first group (Campanya et al., 2019; Gannon et al., 2017; Kelbert et al., 2017; Lucas et al., 2018; Love et al., 2019; Torta et al., 2017, among others) are based on convolving magnetotelluric (MT) impedances (which are experimentally estimated in the region of interest) with ground magnetic fields that are measured at or interpolated from nearby geomagnetic observatories/sites. Since MT responses are involved in computations, this approach implicitly assumes that the source of geomagnetic disturbances (space weather events) is approximated by a plane wave (Chave & Jones, 2012).

Computations of the GEF within the second, most populated, group of papers (Beggan et al., 2013; Bailey et al., 2017, 2018; Divett et al., 2017; Dimmock et al., 2019; Liu et al., 2018; Marshall et al., 2019; Nakamura et al., 2018; Püthe & Kuvshinov, 2013; Püthe et al., 2014; Pokhrel et al., 2018; Rosenqvist & Hall, 2019; Wang et al., 2016, among others) rely on a numerical modeling of the GEF, either with a thin sheet or fully 3-D conductivity models of the Earth. 3-D conductivity models can be compiled using, for instance, results of regional MT surveys or/and exploiting global and regional maps of bathymetry, sediment thickness, etc. One example of such compilation which is relevant to space weather applications is presented in Alekseev et al. (2015).

Common in the second approach is an approximation of the actual source either by idealized current systems, or current systems that are obtained from the data collected at observatories/sites located in the studied regions. Note that most of modelings are performed on a regional scale, with two exceptions: Püthe and Kuvshinov (2013) and Püthe et al. (2014) computed electric (and magnetic) fields globally. Since observatories are sparsely and irregularly distributed around the globe, one can use this approach to reproduce the GEF only from large-scale sources, for example, from those that are responsible for midlatitude and low-latitude signals during geomagnetic storms. However, the highest risk from GICs comes, supposedly, from fast-varying and rather small-scale currents generated in the high-latitude ionosphere during magnetospheric substorms and different impulsive events (Belakhovsky et al., 2019).

The third approach presented in Ivannikova et al. (2018) and Honkonen et al. (2018) allows to simulate electromagnetic (EM) effects from both large-scale and small-scale sources. It also exploits 3-D numerical modeling. However, the source of geomagnetic disturbances is retrieved from the outputs of 3-D magneto-hydrodynamic (MHD) physics-based simulations of near-Earth space. Ivannikova et al. (2018) carried out thin-sheet and 3-D EM modeling for the British Isles region, whereas Honkonen et al. (2018) performed thin-sheet modeling on a global scale. Both studies explore the coastal effect in the GEF using conductivity models with simplified (either laterally homogeneous or thin-sheet) landmass conductivity.

In the current study we use the 3-D EM modeling approach of Ivannikova et al. (2018) to compute the GEF in the eastern United States. Taking St. Patrick's Day geomagnetic storm of March 2015 as an example event, we explore the effects in the GEF arising from conductivity contrasts for various conductivity models of the region, including a realistic 3-D model, obtained from inversion of the EarthScope MT data (Kelbert et al., 2011). We also discuss the difference between the GEF induced by the laterally varying MHD source employed in this paper and the GEF calculated using the plane wave modeling approach.

2. Methods

2.1. Ground EM Field Modeling

We compute the electric, $\mathbf{E}(t, \mathbf{r})$, and magnetic, $\mathbf{B}(t, \mathbf{r})$, fields for a given Earth's conductivity distribution $\sigma(\mathbf{r})$ and a given inducing source $\mathbf{j}^{ext}(t, \mathbf{r})$, where t stands for time and $\mathbf{r} = (x, y, z)$ for position vector. These fields obey Maxwell's equations that are written in the time domain as

$$\frac{1}{\mu_0} \nabla \times \mathbf{B} = \sigma \mathbf{E} + \mathbf{j}^{ext}, \tag{1}$$

$$\nabla \times \mathbf{E} = -\frac{\partial \mathbf{B}}{\partial t}, \tag{2}$$

where μ_0 is the magnetic permeability of free space. We solve equations (1) and (2) numerically using the following three-step procedure:

1. The inducing source $\mathbf{j}^{ext}(t, \mathbf{r})$ is transformed from time to frequency domain with a fast Fourier transform (FFT).
2. Maxwell's equations in the frequency domain

$$\frac{1}{\mu_0} \nabla \times \mathbf{B} = \sigma \mathbf{E} + \mathbf{j}^{ext}, \tag{3}$$

$$\nabla \times \mathbf{E} = i\omega \mathbf{B}, \tag{4}$$

   are numerically solved for the corresponding angular frequencies $\omega = 2\pi f$, using the scalable 3-D EM forward modeling code *extrEMe* (Kruglyakov et al., 2016), based on a contracting integral equation approach (Pankratov et al., 1995). Frequencies f range between $\frac{1}{L}$ and $\frac{1}{2\Delta t}$ where L is the length of the (input) times series of the inducing current $\mathbf{j}^{ext}(t, \mathbf{r})$, and Δt is the sampling rate of this time series. In this study Δt is 1 min, and L is 48 hr.
3. $\mathbf{E}(t, \mathbf{r})$ (and $\mathbf{B}(t, \mathbf{r})$) are obtained with an inverse FFT of the frequency domain fields.

2.2. Construction of 3-D Conductivity Models

We construct a number of (Cartesian) 3-D models of the region with the aim to explore how different conductivity distributions influence the GEF in the region. The first model includes a bathymetrically nonuniform
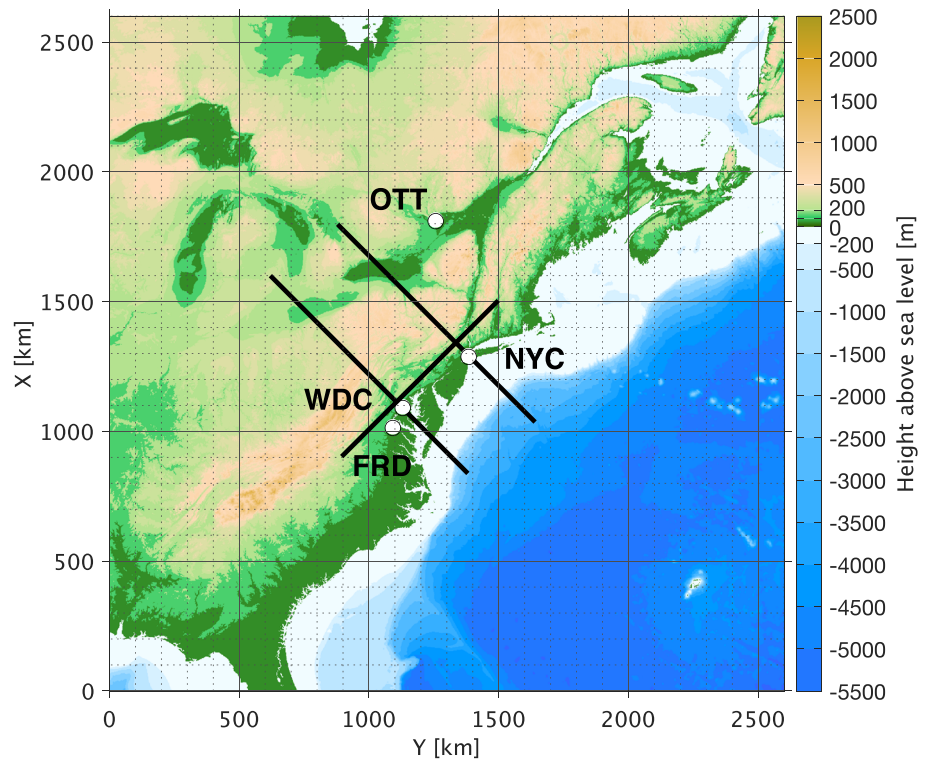
Figure 1. Topography/bathymetry map of the eastern United States and surrounding areas, constructed using NOAA's ETOPO1 Global Relief Model. Locations of New York City (NYC), Washington, DC (WDC), and geomagnetic observatories Fredericksburg (FRD) and Ottawa (OTT) are marked with circles. The bold black lines denote the profiles along which the results are demonstrated in a number of figures.

ocean and a landmass of uniform conductivity. Here under the landmass we understand the upper crust which goes down to the maximum depth of the ocean (5.8 km in the considered region). The landmass and the ocean comprise the 3-D part of the model which is underlain by a crust and mantle with a 1-D conductivity distribution. The first model is used to study the so-called coastal effect. Hereafter we will use the abbreviation UCL (Uniform Conductivity of Landmass) for this model. To specify the conductivity distribution within the ocean, we use publicly available bathymetry data from National Oceanic and Atmospheric Administration (NOAA)'s ETOPO1 Global Relief Model (Amante & Eakins, 2009). The data are provided in geographic coordinates with resolution of 1×1 arc-minute. The Transverse Mercator map projection is used to convert the data into Cartesian geometry. Figure 1 demonstrates the topography/bathymetry map of the region. The conductivity of the seawater in the model is set to 3.2 S/m and does not vary in the course of modeling. What is varied during simulations in the UCL model is the conductivity of the landmass and the 1-D conductivity distribution in the underlying crust and mantle. Three values of the landmass conductivity are considered: 0.1, 0.01, and 0.001 S/m. As for the underlying crust and mantle, we tried two (global) conductivity models that are shown in Figure 2. One is the model of Grayver et al. (2017) obtained by joint inversion of tidal magnetic signals and C-responses. The other is the model of Püthe et al. (2015) obtained by inversion of C-responses only. Note that different data sets and different algorithms were used to obtain the corresponding C-responses.

More details on the UCL model construction are as follows. First we note that as far as we exploit integral equation approach to calculate the EM field, the modeling domain is confined to the 3-D part of the model only. The vertical size of the domain corresponds to the maximum depth of the ocean in the considered region (5.8 km). Elevations above sea level are ignored. The 3-D volume is discretized vertically by eight layers of uniform thickness of 0.725 km. Laterally, it is discretized by 512×512 cells of uniform size: 5.1 km in both directions. The 3-D part of the UCL model is shown in Figure 3. Outside the 3-D volume, at depths between 0 and 5.8 km, the conductivity is assumed to be uniform and is set to the corresponding conductivity of the landmass.
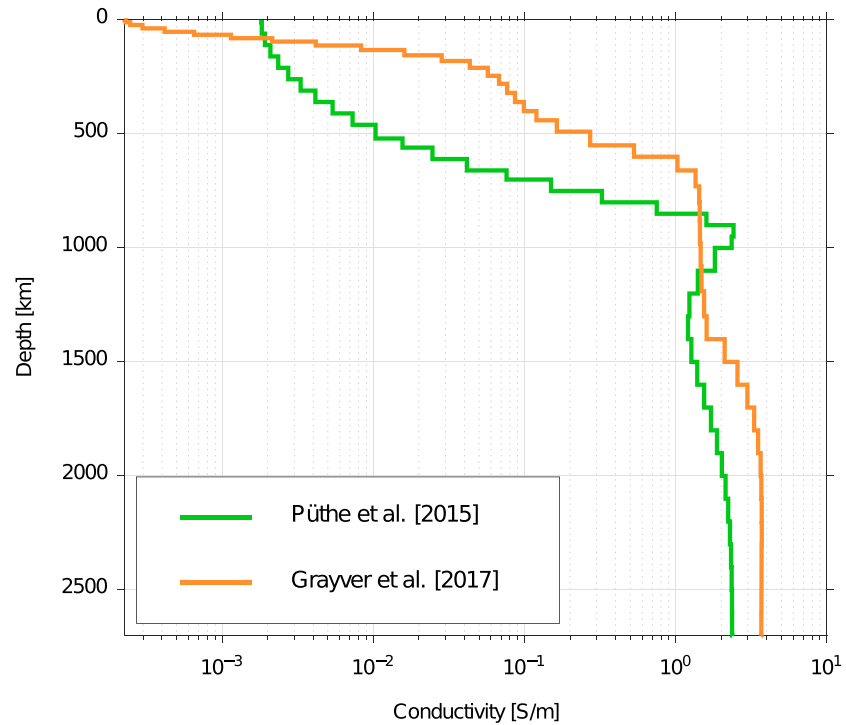
Figure 2. Global 1-D conductivity profiles derived by Grayver et al. (2017) and Püthe et al. (2015) and used in this study.

The second 3-D conductivity model has laterally and vertically inhomogeneous landmass conductivity distribution. It mimics the 3-D conductivity distribution of the eastern United States (APPL model, named after the Appalachian Mountains—the key geologic structure of this region) recovered by inversion of Earth-Scope MT data. This 3-D conductivity distribution was obtained by means of 3-D EM inversion code *ModEM* (Kelbert et al., 2014) using data from 240 EarthScope Transportable Array (TA) long-period MT sites (Kelbert et al., 2019). The original APPL model fits the MT data reasonably well: the normalized root-mean-square misfit achieved in the process of inversion is 1.5. In the course of preparing the second model the original APPL conductivity distribution was downsampled, in order to reduce computational loads: the resulting modeling region goes vertically down to 400 km depth and is discretized vertically by 18 layers: 8 upper layers of 0.725 km thickness, 4 intermediate layers of 23.5 km thickness, and 6 lower layers of 50 km thickness. The 3-D part of this model is shown in Figure 4. Laterally, the modeling region is, again, discretized by 512×512 cells of uniform size: 5.1 km in both directions.

Figure 3. Conductivity distribution in the UCL model: (a) map view of the first layer of 3-D part of the model; (b) oblique view of 3-D part of the model. The vertical exaggeration in plot (b) is 100 times.
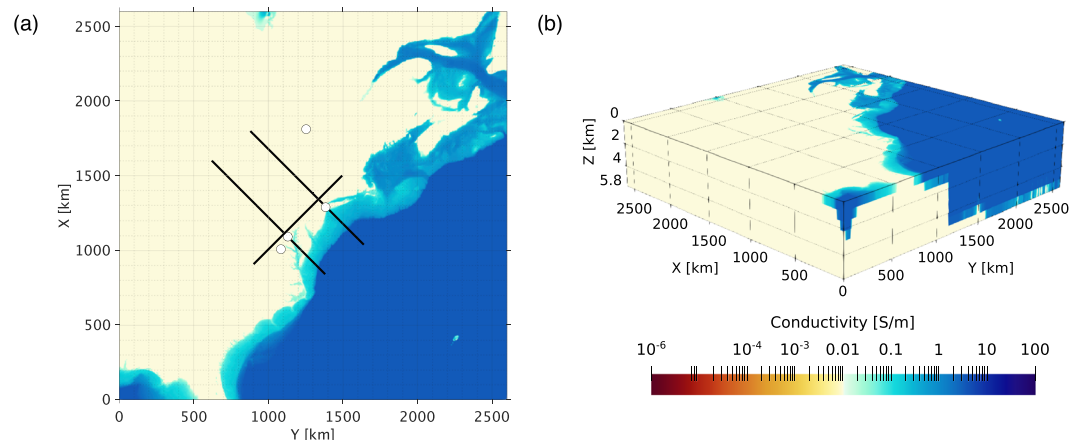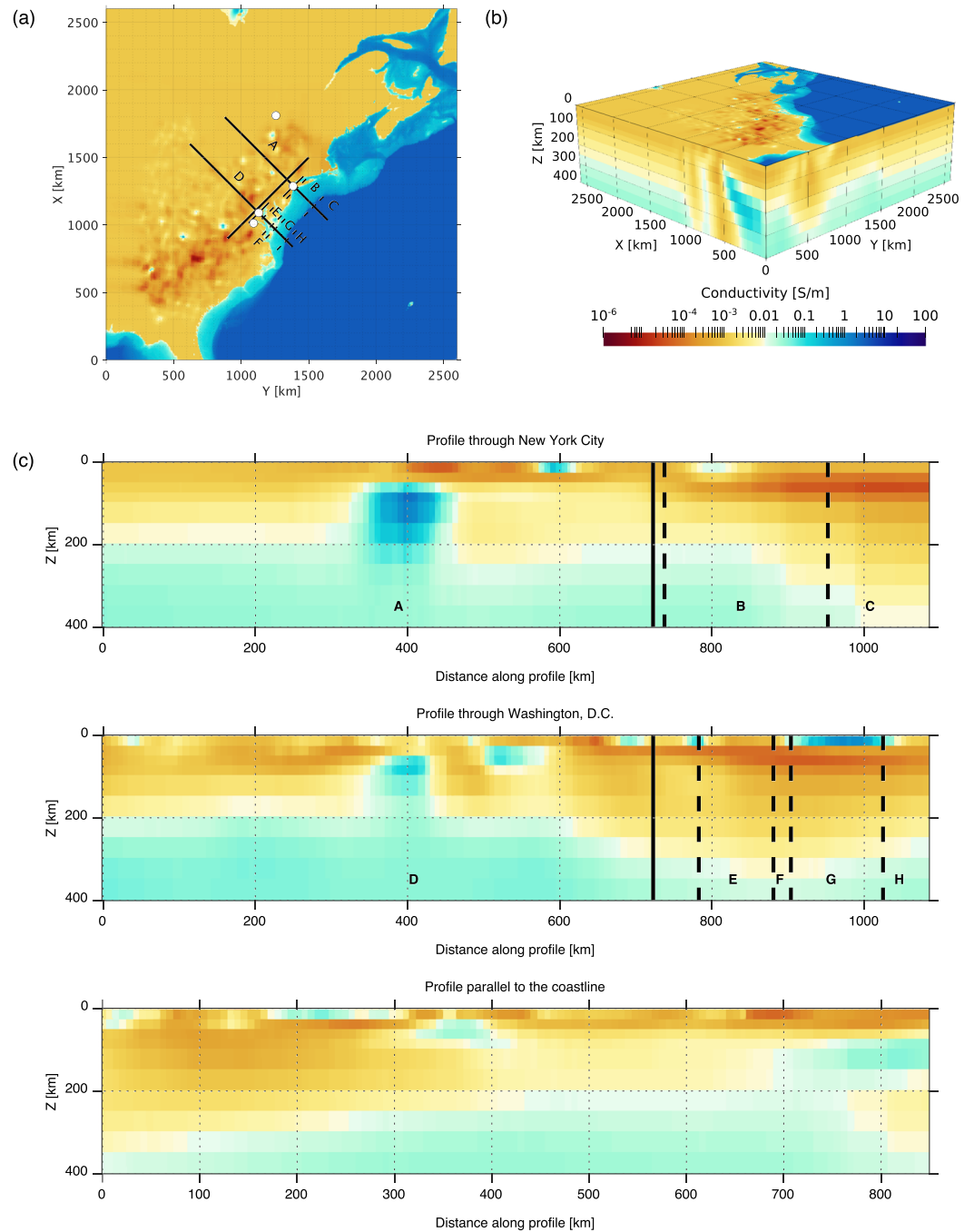
Figure 4. Conductivity distribution in the APPL model: (a) map view of the first layer of 3-D part of the model; (b) oblique view of 3-D part of the model; (c) cross sections through the model along NYC, WDC, and coastal profiles. The vertical exaggeration in plot (b) is 2 times. Solid vertical lines in (c) mark the centers of the cities. Dashed vertical black lines mark the coasts and the boundaries between shallow and deep sea. For NYC profile: A = land part of the profile, B = shallow sea, C = deep sea. For the WDC profile: D, F = land parts of the profile, E = Chesapeake Bay, G = shallow sea, H = deep sea.

We also construct two auxiliary conductivity models, APPL2 and APPL3, in order to quantitatively study: (a) the effects arising from landmass conductivity inhomogeneities and; (b) the coastal effect in the presence of a heterogeneous landmass. Specifically, the APPL2 model consists of the layered structure coinciding with the background 1-D profile of the APPL model (the initial stratified model of the APPL 3-D model) and bathymetrically nonuniform ocean. By comparing modeling results obtained in the APPL and APPL2 models, we are able to assess the effects arising due to 3-D landmass conductivity distribution. The APPL3 model is constructed by replacing the ocean in the APPL model with the APPL 1-D background conductivity distribution; by comparing modeling results from the APPL and APPL3 models the coastal effect in the APPL model can be assessed. Figure S1 in supporting information demonstrates 3-D parts of these models.

2.3. Source Model Construction

We construct the source model (inducing current, $\mathbf{j}^{ext}(t, \mathbf{r})$, in equation (1)) for the 2-day time period from 00:00 UT, 17 March 2015 to 23:59 UT, 18 March 2015 when the so-called St. Patrick's Day geomagnetic storm occurred. This is the largest geomagnetic storm in the 24th solar cycle: disturbance storm time (Dst) index reached −228 nT.

The source model is constructed on the base of outputs of the Space Weather Modeling Framework (SWMF) developed at the University of Michigan (Toth et al., 2005, 2012). The input of this MHD model are solar wind parameters (density, temperature, velocity, and magnetic field) measured at satellites located at L1 Lagrangian point, such as Advanced Composition Explorer (ACE) or Deep Space Climate Observatory (DSCOVR). The outputs are time-varying 3-D currents in the magnetosphere, horizontal currents in the ionosphere and field-aligned currents (FAC) flowing between the magnetosphere and the ionosphere.

The SWMF includes various physics-based numerical models. The dynamic response of the Global Magnetosphere (GM) to changing solar wind conditions is predicted using the Block-Adaptive-Tree-Solarwind-Roe-Upwind-Scheme (BATS-R-US) global MHD code (Powell et al., 1999). The inner magnetosphere (IM) dynamics is simulated using the Rice Convection Model (RCM) coupled to BATS-R-US (De Zeeuw et al., 2004). The Ionospheric Electrodynamics (IE) is simulated by a two-dimensional electrostatic potential solver that obtains the FAC from the GM and employs a statistical auroral ionosphere conductance model (Ridley Ionosphere Model (RIM), Ridley et al., 2004).

3-D currents in the magnetosphere, horizontal currents in the ionosphere, and the FAC obtained by SWMF are then used to calculate (through the Biot-Savart law) external magnetic field perturbations $\mathbf{B}^{ext}$ at the ground. This is done using *CalcDeltaB* tool (Rastätter et al., 2014). Time series of the external magnetic field are calculated globally at $5° \times 5°$ spatial grid with 1-min sampling rate and further converted into current function Ψ (see Ivannikova et al., 2018, for more details on the conversion procedure). Note that the inducing source $\mathbf{j}^{ext}$ has a form of spatially distributed electric current flowing in a thin shell above the Earth. This means, that $\mathbf{j}^{ext}$ degenerates to the sheet current density $\mathbf{J}^{ext}$ flowing in a thin shell of radius $r = a+$:

$$\mathbf{J}^{ext} = -\mathbf{e}_r \times \nabla_\perp \Psi. \tag{5}$$

Here $\mathbf{e}_r$ is radial (outward) unit vector, $\nabla_\perp$ is surface gradient, and a is the radius of the Earth. We then project the global current function Ψ from spherical to Cartesian geometry onto a region of interest and interpolate the resulting regional current function onto a regular grid. Finally, we obtain the regional sheet current density $\mathbf{J}^{ext}$ by numerical differentiation of the regional current function by means of equation (5). This sheet current density is used to form inducing current $\mathbf{j}^{ext}$ as

$$\mathbf{j}^{ext} = \delta(z - 0+)\mathbf{J}^{ext}, \tag{6}$$

where $\delta(z - 0+)$ is Dirac's delta function.

It is important to note here that the regional current sheet covers the region that is twice as large in each lateral direction as the modeling region. This is done to diminish edge effects that could arise due to cropping of the global source.

The SWMF run, results of which were used in the current study, was performed at NASA's Community Coordinated Modeling Center (CCMC) at the Goddard Space Flight Center. Details and results of the run are available at the CCMC website (https://ccmc.gsfc.nasa.gov, run number Lois_Smith_040815_1). The snapshots of the constructed sheet current system for 12:31 and 12:59 UT on 17 March 2015 (when substantial
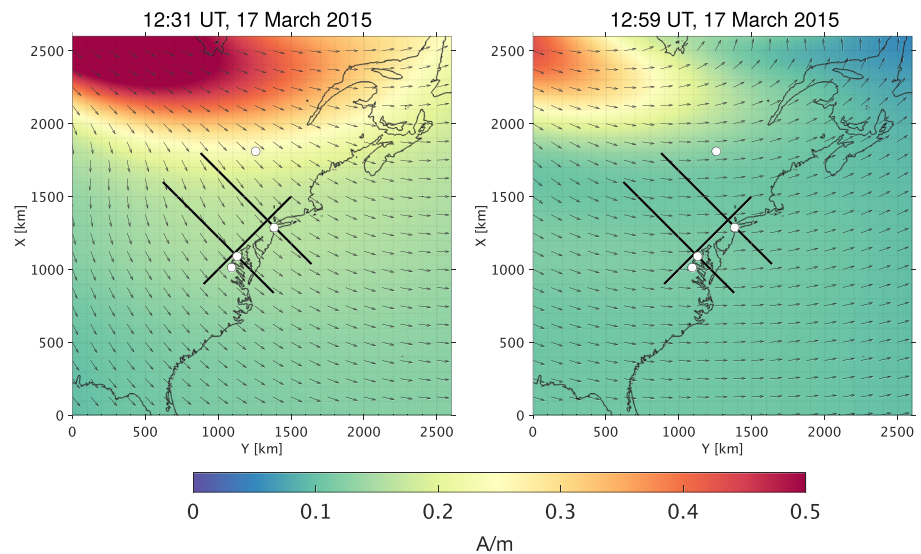
Figure 5. Snapshots of the equivalent current magnitude and direction at the surface of the Earth at 12:31 UT (left) and 12:59 UT (right) on 17 March 2015.

intensification of the electric field was observed) are shown in Figure 5. Hereinafter the results are shown only for these time instants.

3. Results

Most of the results in this section are demonstrated along three profiles. Two profiles (parallel to each other) go through New York City (NYC) and Washington, DC (WDC), and are roughly perpendicular to the coastline (see Figure 1). Hereinafter we will denote these profiles as NYC and WDC profiles, respectively. The third profile is roughly parallel to the coastline (see, again, Figure 1). Henceforth we will refer to this profile as the coastal profile. Moreover, in the main text of the paper, we will demonstrate the GEF components that are directed along these profiles. The following nomenclature is then introduced for these components: we denote as $E_\perp$ the GEF component that is directed along NYC and WDC profiles, and as $E_\parallel$ the component directed along the coastal profile. Essentially, this nomenclature means that $E_\perp$ and $E_\parallel$ are components roughly perpendicular and parallel to the coastline. Complementary components, $E_\parallel$ for NYC and WDC profiles and $E_\perp$ for the coastal profile, are presented in the supporting information. Note also that all results are calculated at the surface of the Earth.

3.1. Modeling Coastal Effect in a Simplified 3-D Model

As is well known, the coastal effect is the anomalous behavior of the EM field arising from the lateral conductivity contrast between the ocean and the land. It was previously mostly studied in the context of MT (Fischer & Weaver, 1986; Parkinson & Jones, 1979; Weaver & Dawson, 1992, among others) and geomagnetic depth sounding (Kuvshinov et al., 1999; Kuvshinov, 2008, among others) researches. This effect in the GEF was also discussed in a number of studies in connection with space weather research (Gilbert, 2005; Honkonen et al., 2018; Ivannikova et al., 2018; Liu et al., 2018; Nakamura et al., 2018; Püthe & Kuvshinov, 2013, among others). Usually, it is quantitatively assessed by comparing results of 3-D and 1-D computations, where 3-D modeling aims at reproducing effects from lateral ocean/land conductivity contrasts. Note that since we are interested in exploring the coastal effect on land, the 1-D modeling exploits a 1-D conductivity profile (either from Püthe et al., 2015, or from Grayver et al., 2017) overlain by a homogeneous upper layer of landmass conductivity. Since the ocean is not included in 1-D conductivity models, comparison of 3-D and 1-D modeling results will be demonstrated only for land areas. Note also that, in spite of the fact that a purely 1-D conductivity model is used during 1-D calculations, the lateral inhomogeneity of the inducing current (source) makes the problem fully 3-D.

The left plots in Figure 6 show the spatial distribution of the GEF at 12:59 UT calculated in 3-D UCL model with laterally homogeneous landmass conductivity of 0.01 S/m and the 1-D conductivity profile from Püthe et al. (2015). The right plots present the difference between 3-D and 1-D modeling results. As expected,
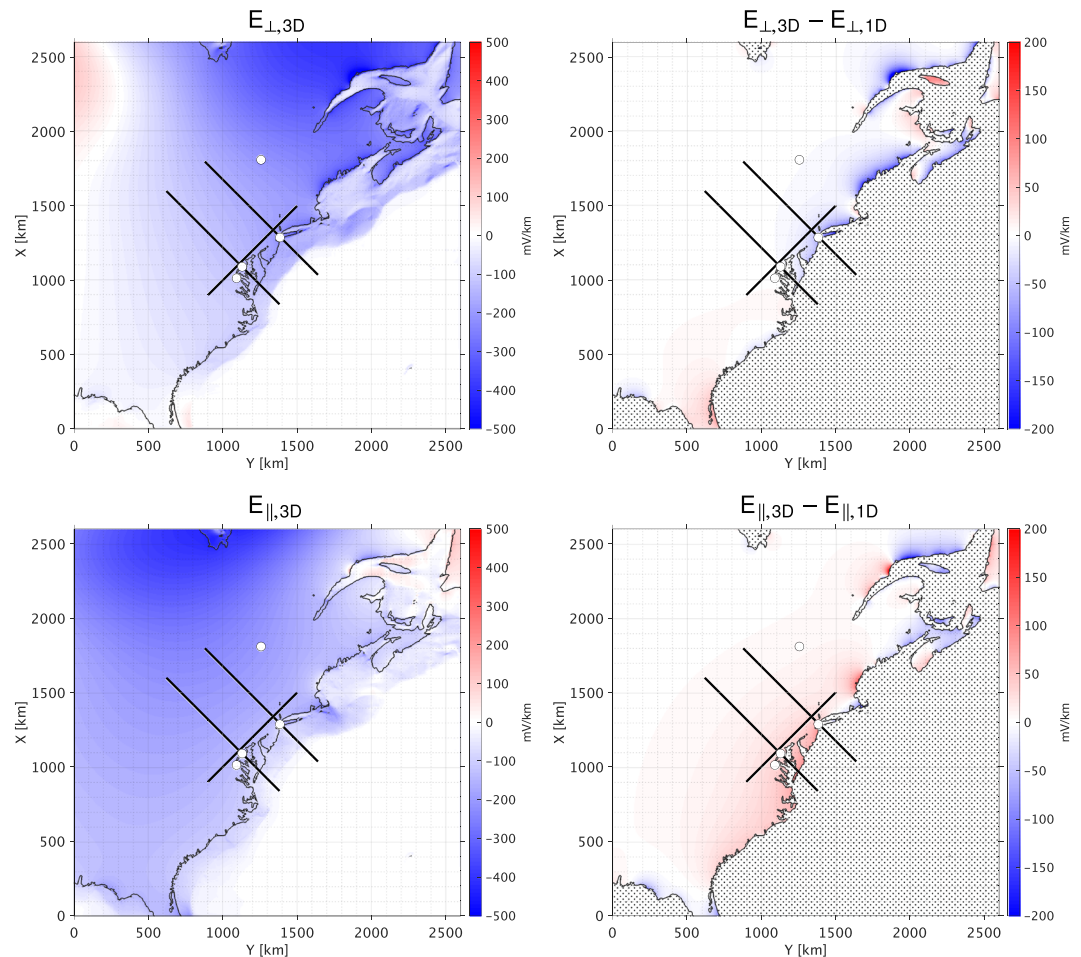
Figure 6. (left) Snapshots of the GEF components perpendicular (top) and parallel (bottom) to the coastline calculated in the UCL (3-D) model. (right) The difference between results of 3-D and 1-D modeling (the difference is demonstrated only for land areas). The results are shown at 12:59 UT on 17 March 2015. The calculations were carried out for models with homogeneous landmass conductivity of 0.01 S/m and 1-D conductivity profile from Püthe et al. (2015). Note different color scales in left and right plots.

the difference is maximum in the coastal areas and decreases on land farther from the coast. For this time instant the noticeable difference between 3-D and 1-D modeling results for the GEF component parallel to the coastline extends over larger areas compared to the component perpendicular to the coastline. The situation is, however, opposite at 12:31 UT (see Figure S2 in the supporting information).

3.1.1. Varying 1-D Crust and Mantle Conductivity

To demonstrate the coastal effect in more detail, Figure 7 presents $E_\perp$ along NYC and WDC profiles and $E_\parallel$ along the coastal profile. The results are presented for two trial 1-D profiles and two time instants. As is seen, the electric field is significantly affected by the ocean/land conductivity contrast. It is generally strongly amplified at the coasts, and the anomalous behavior (coastal effect) propagates up to several hundred kilometers on land. The actual behavior apparently depends on the geometry of the coastline and on the spatiotemporal behavior of the source. Figure S3 in the supporting information demonstrates in a similar manner $E_\parallel$ along NYC and WDC profiles and $E_\perp$ along the coastal profile. Large localized amplifications are usually absent in $E_\parallel$, but significant differences between 3-D and 1-D modeling results can extend even over larger areas on land compared to $E_\perp$. These features of the coastal effect in the case of a nonuniform source are expectedly consistent with the ones, obtained for MT modeling in the earlier studies (Fischer, 1979; Weaver, 1963).

The results for the two trial 1-D conductivity profiles (shown in Figure 2) do not significantly differ in terms of maximum amplitudes of the GEF due to the coastal effect, but differences in the background model
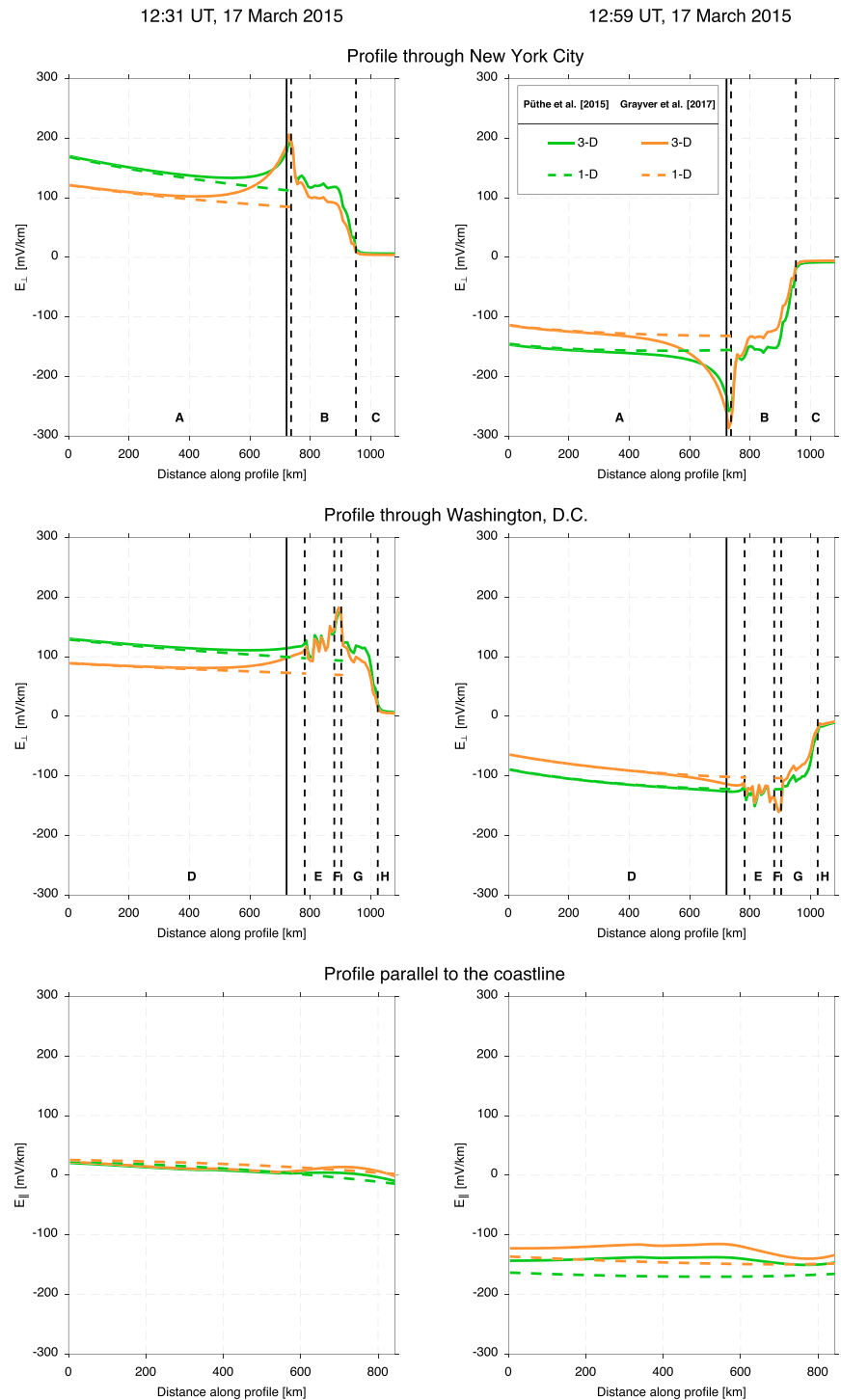
Figure 7. The GEF along three profiles calculated using different 1-D conductivity models. (top and middle) The GEF component perpendicular to the coastline along NYC and WDC profiles, respectively. (bottom) The GEF component parallel to the coastline along the coastal profile. GEFs are calculated in the UCL (3-D) and 1-D models. The results are presented at two, 12:31 (left) and 12:59 (right), time instants. Green curves represent the results obtained for models with 1-D conductivity profile from Püthe et al. (2015); orange curves are for models with 1-D profile from Grayver et al. (2017). Solid vertical lines mark the centers of the cities. Dashed vertical black lines mark the coasts and the boundaries between shallow and deep sea. For NYC profile: A = land part of the profile, B = shallow sea, C = deep sea. For the WDC profile: D, F = land parts of the profile, E = Chesapeake Bay, G = shallow sea, H = deep sea. The results of 1-D modeling are demonstrated only for land areas A, D, and F and the coastal profile. The calculations were carried out for models with homogeneous landmass conductivity of 0.01 S/m.
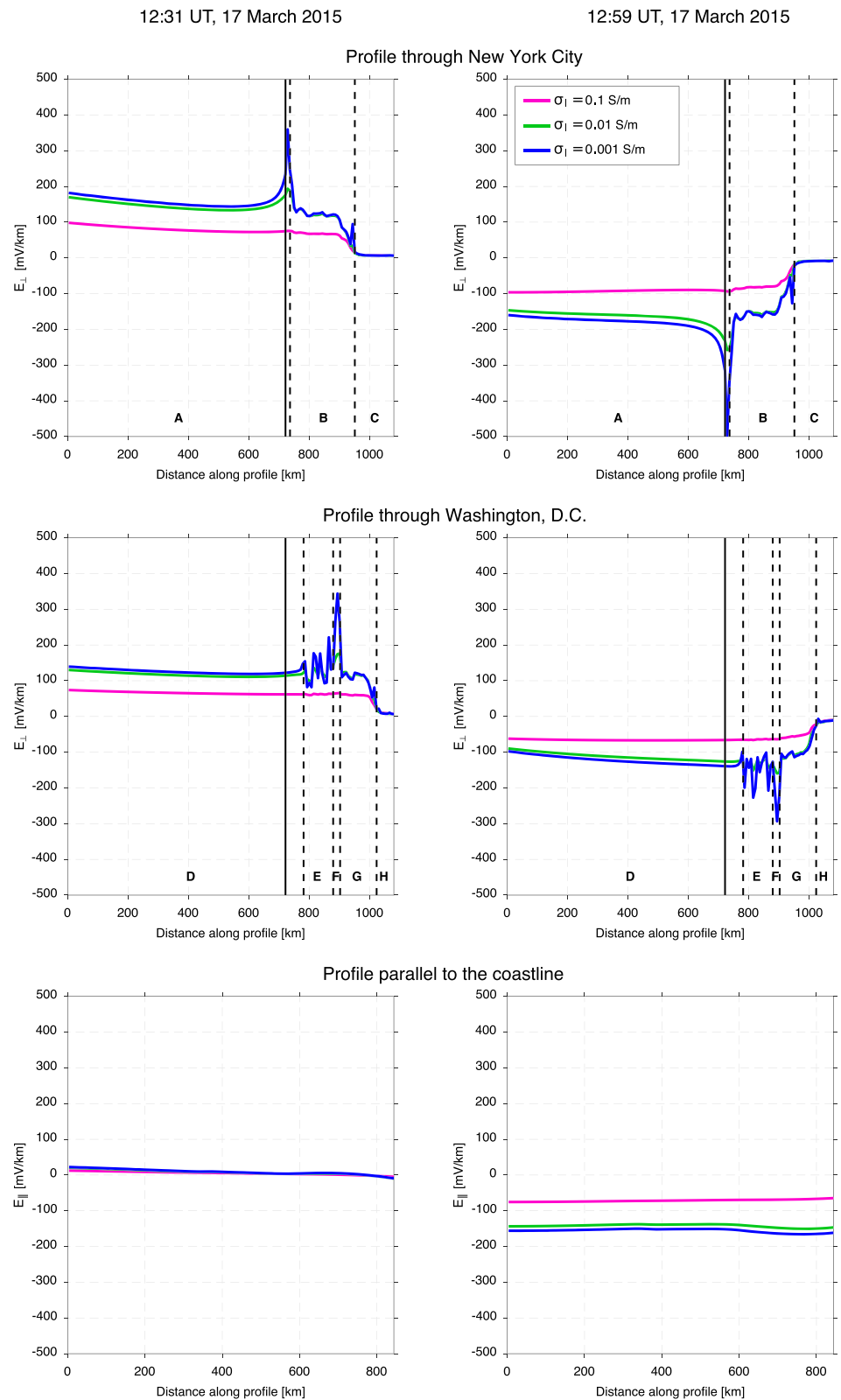
Figure 8. The GEF along three profiles calculated using different conductivities of homogeneous landmass. The caption is similar to the one in Figure 7.
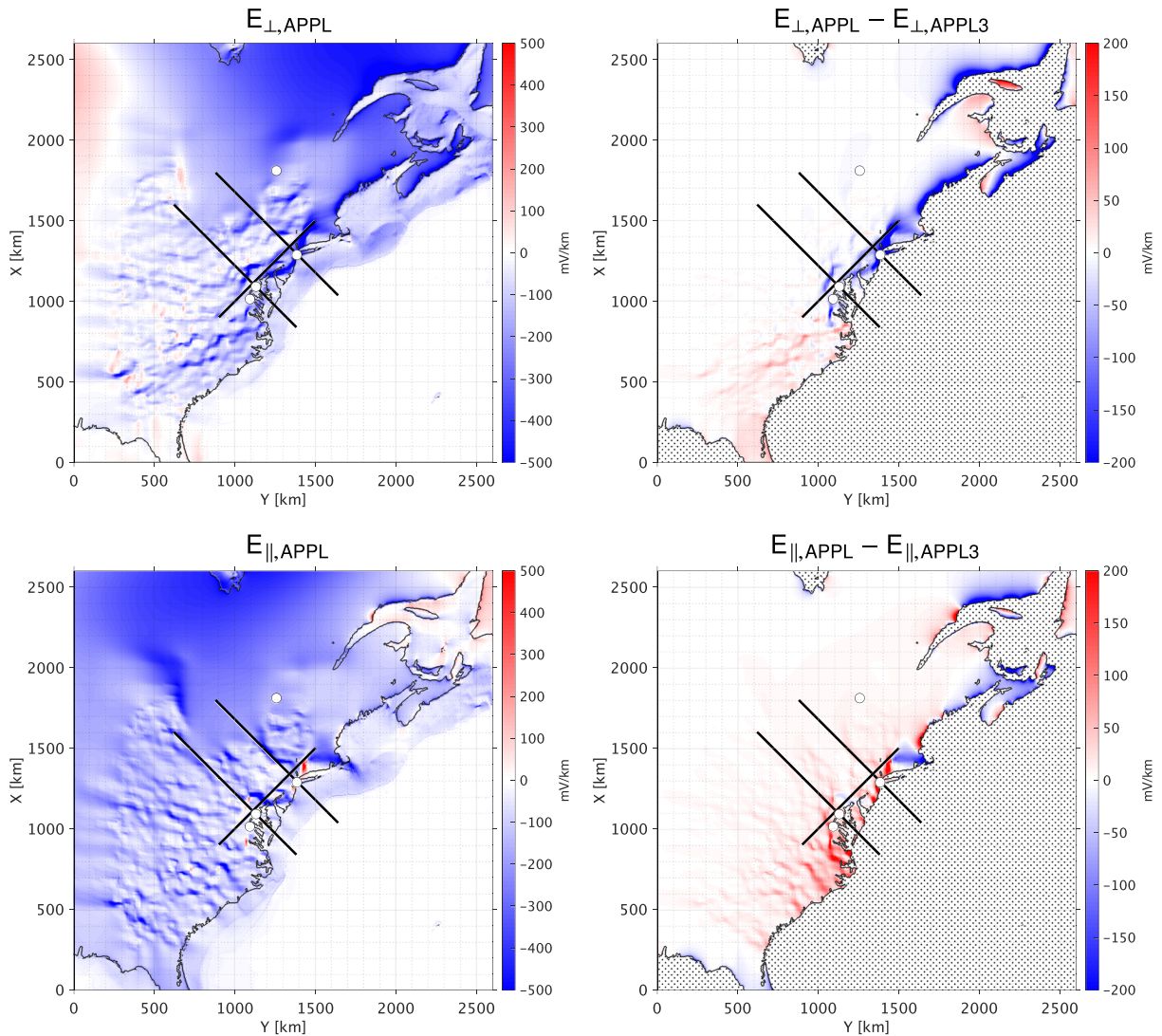
Figure 9. (left) Snapshots of the GEF components perpendicular (top) and parallel (bottom) to the coastline calculated in the APPL model. (right) The difference between results for the APPL and APPL3 (no ocean) models (the difference is demonstrated only for land areas). The results are shown at 12:59 UT on 17 March 2015. The calculations were carried out for models with 1-D conductivity profile from Püthe et al. (2015). Note different color scales in left and right plots.

expectedly influence the behavior of the GEF farther from the coast (Figure 7). The magnitudes of the GEF for 1-D model derived by Püthe et al. (2015) usually exceed the corresponding magnitudes for the model derived by Grayver et al. (2017) about 20-30%.

3.1.2. Varying the Uniform Landmass Conductivity

In order to further study the influence of the lateral conductivity contrast between the ocean and the continent on the intensity of the coastal effect, we carried out computations in the models with three trial values of landmass conductivity: 0.1, 0.01, and 0.001 S/m. Note that, in this model experiment, the 1-D conductivity model which underlies the ocean and the continent is that derived by Püthe et al. (2015).

Figure 8 shows $E_\perp$ along NYC and WDC profiles and $E_\parallel$ along the coastal profile. The results are presented for the aforementioned three conductivity models and, again, for two time instants. There is almost no amplification of the GEF near the coast in the model with landmass conductivity of 0.1 S/m. For models with landmass conductivities of 0.01 and 0.001 S/m, the GEF is noticeably amplified at the coast, and, furthermore, the peak coastal electric field values in the model with conductivity of 0.001 S/m are about 1.5–2 times higher compared to that obtained from the model with conductivity of 0.01 S/m. Figure S4 in the supporting information demonstrates in a similar manner $E_\parallel$ along NYC and WDC profiles and $E_\perp$ along the

coastal profile. Comparing results in Figures 8 and S4, one can see that the coastal effect is overall more pronounced in $E_\perp$ than in $E_\parallel$ component.

3.2. Effects from Coastal and Landmass Heterogeneities in a Realistic 3-D Model

So far we have discussed the coastal effect in the GEF using simplified 3-D model in which the landmass conductivity does not vary laterally and vertically. In this section we present results calculated in the APPL 3-D model, which comprises a realistic inhomogeneous landmass. The left plots in Figure 9 show the spatial distribution of the GEF at 12:59 UT calculated in the APPL model, whereas the right plots present the difference between results calculated in the APPL and APPL3 3-D models. Recall that the APPL3 model does not contain the ocean (see details about both models in section 2.2). It is apparent here how sophisticated the GEF behavior is with the realistic 3-D conductivity distribution of the region. The difference between the APPL and APPL3 modeling results is far more complex than the difference between 3-D and 1-D modeling results obtained in the ULC model demonstrated in Figure 6. The coastal effect also propagates well inland, but the largest differences between modeling results do not necessarily appear at the coasts. It is clear that effects from landmass 3-D conductivity inhomogeneities interfere with effects from the conductivity contrast between the ocean and the land. Figure S5 in the supporting information shows results at 12:31 time instant and reveals similar behavior.

Figure 10 presents the GEF for three (APPL, APPL2, and APPL3) 3-D models along NYC, WDC, and coastal profiles for two time instants. Recall that landmass conductivity in the APPL2 does not vary laterally. The presence of landmass 3-D inhomogeneities dramatically changes the behavior of the GEF, which displays large amplitude in a short spatial scale. These variations are mostly due to subsurface local and crustal structures. Note that subsurface local inhomogeneities are introduced by 3-D MT inversion to account for galvanic effects (Jiracek, 1990) in MT impedances. It is worth mentioning here that a part of NYC profile (the first 250 km) is located in the area unconstrained by MT data, for which we do not have inversion results (see Figures 4a and 4c). That is why the behavior of the GEF for the APPL model for the first 250 km of the profile is similar to the behavior of the GEF for the APPL2 model. The difference between APPL and APPL3 results reflects the coastal effect in the presence of inhomogeneous landmass. From results at NYC and WDC profiles, one can deduce that the difference between the APPL and APPL3 $E_\perp$ is substantial at a distance of approximately 100 km from the coast, and this difference can be very large (for NYC profile the peak APPL $E_\perp$ is a few [up to 5] times larger compared to the APPL3 $E_\perp$). $E_\parallel$ along the coastal profile, shown in the lower plots, is also affected by the presence of the ocean but, seemingly, not as strongly as $E_\perp$ along NYC and WDC profiles. Figure S6 in the supporting information demonstrates in a similar manner $E_\parallel$ along NYC and WDC profiles and $E_\perp$ along the coastal profile. It is seen that $E_\parallel$ along NYC and WDC profiles is less affected by the coastal effect than $E_\perp$ along the same profiles.

In order to demonstrate the spatial distribution of the storm time GEF in the region in more detail, we utilize the concept of maps of the GEF amplitude and direction that was previously used by Love et al. (2018a, 2018b, 2019). Specifically, we present the GEF at locations of MT sites for time instants when maximum amplitudes of the modeled GEF during the 17–18 March 2015 geomagnetic storm are detected. We chose MT sites from which the data were used to develop the APPL model and sites used in the study of Love et al. (2019).

Figure 11 demonstrates corresponding maps computed in the APPL and APPL2 models. Results for the APPL2 model show clear systematic behavior: the GEF is driven by the inducing current systems and influenced by the presence of conductivity contrasts between the ocean and the land. The GEF is amplified at the coasts and in the northern areas where the source of excitation is typically stronger. The coastal effect in the APPL model is not as obvious as in the case of the APPL2 model. It manifests itself in the GEF direction at the coasts rather than in the GEF amplification. The GEF in the APPL model is strongly influenced by large lateral contrasts in subsurface conductivity distribution: very low conductivities beneath the Piedmont and Coastal Plain physiographic provinces and high conductivities under the Appalachian Mountains (Kelbert et al., 2019; Murphy & Egbert, 2017). These large-scale geologic structures have clear systematic control over the GEF behavior in this region. MT sites in Figure 11 are separated into two groups: those that were used and those that were not used for the APPL model construction. In general our modeling results agree well with results of Love et al. (2019) in terms of the GEF amplification and direction for the sites that were used in both studies. The GEF amplitudes in our case are smaller compared to results of Love et al. (2019) (in their case amplitudes reach 40 V/km) due to the fact that we carried out modeling for a single geomagnetic
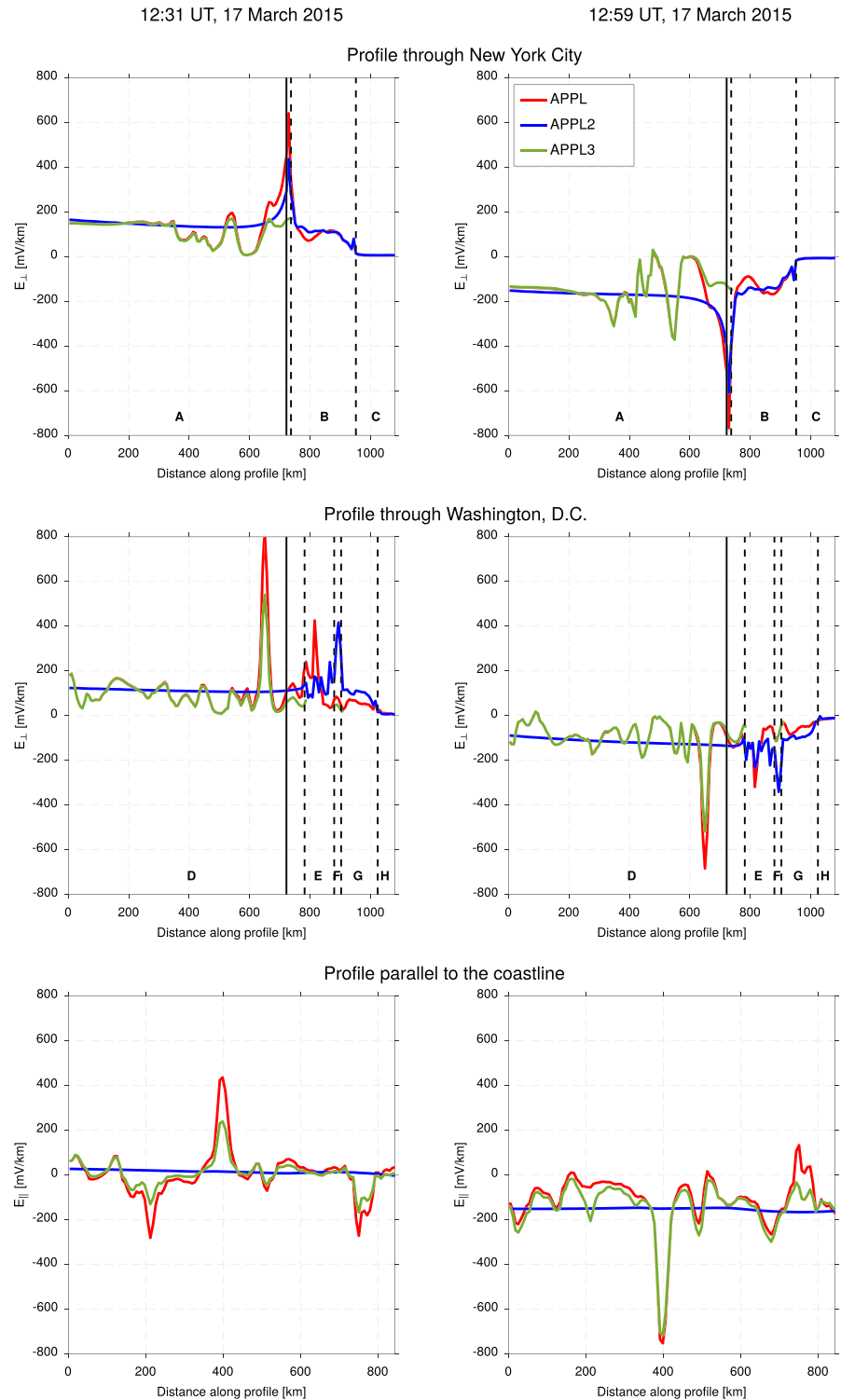
Figure 10. The GEF along three profiles calculated using the APPL, APPL2 (with laterally homogeneous landmass conductivity) and APPL3 (no ocean) models. (top and middle) The GEF component perpendicular to the coastline along NYC and WDC profiles, respectively. (bottom) The GEF component parallel to the coastline along the coastal profile. The results are presented at two, 12:31 (left) and 12:59 (right), time instants. Solid vertical black lines mark the centers of the cities. Dashed vertical black lines mark the coasts and the borders between shallow and deep sea. In the case of NYC profile: A = land part of the profile, B = shallow sea, C = deep sea. For WDC profile: D, F = land parts of the profile, E = Chesapeake Bay, G = shallow sea, H = deep sea. The results for the APPL3 model are demonstrated only for land areas A, D, and F and the coastal profile.
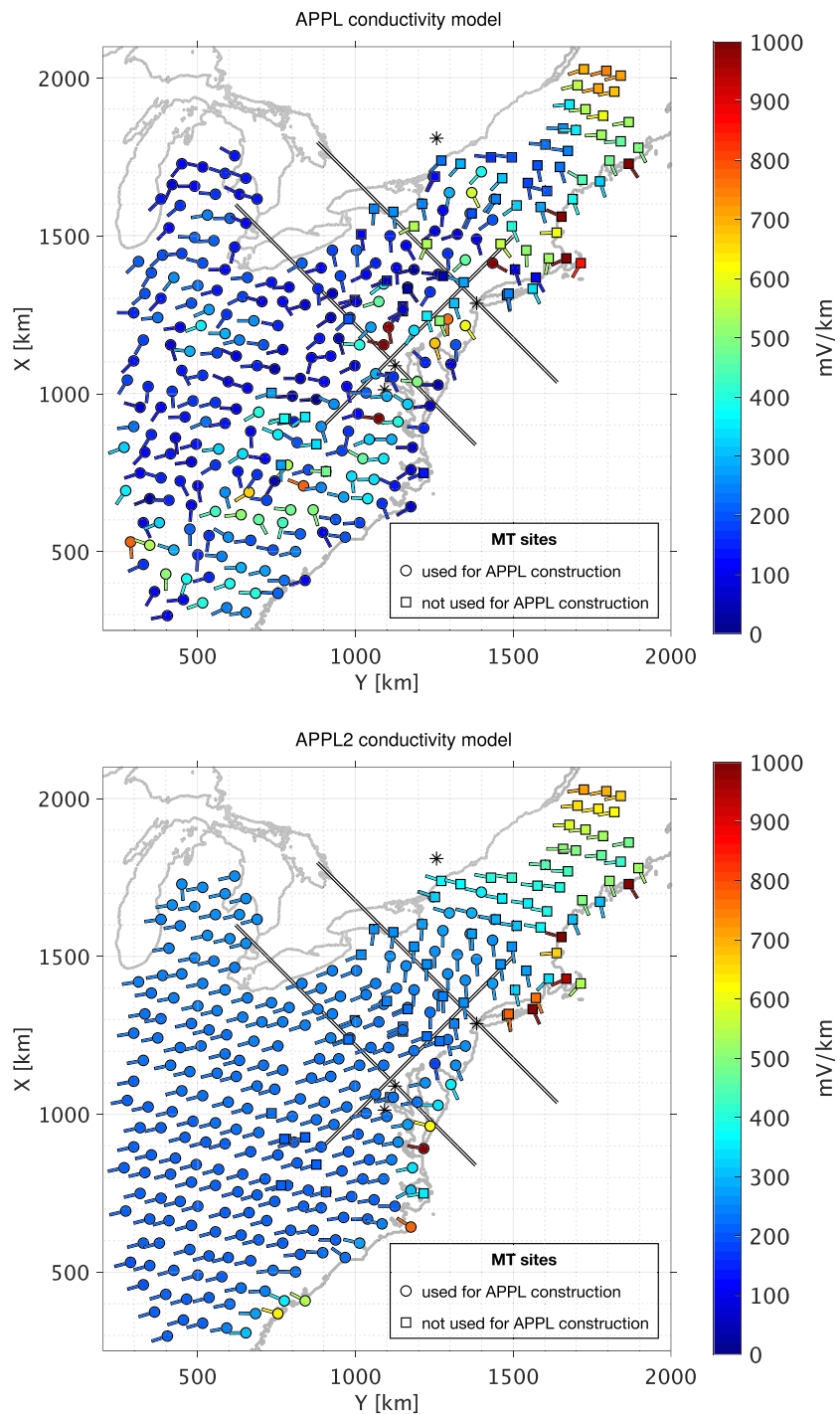
Figure 11. Maps of amplitude and direction of the GEF at locations of MT sites for time instants when maximum amplitudes of the modeled GEF during the 17–18 March 2015 geomagnetic storm are detected. (top and bottom) Results computed for the APPL and APPL2 (with laterally homogeneous landmass conductivity) models, respectively. Sites that were used to construct the APPL model are marked with circles. Sites that were not used for the APPL model construction are marked with squares. Locations of WDC, NYC, FRD, and OTT are marked with asterisks.
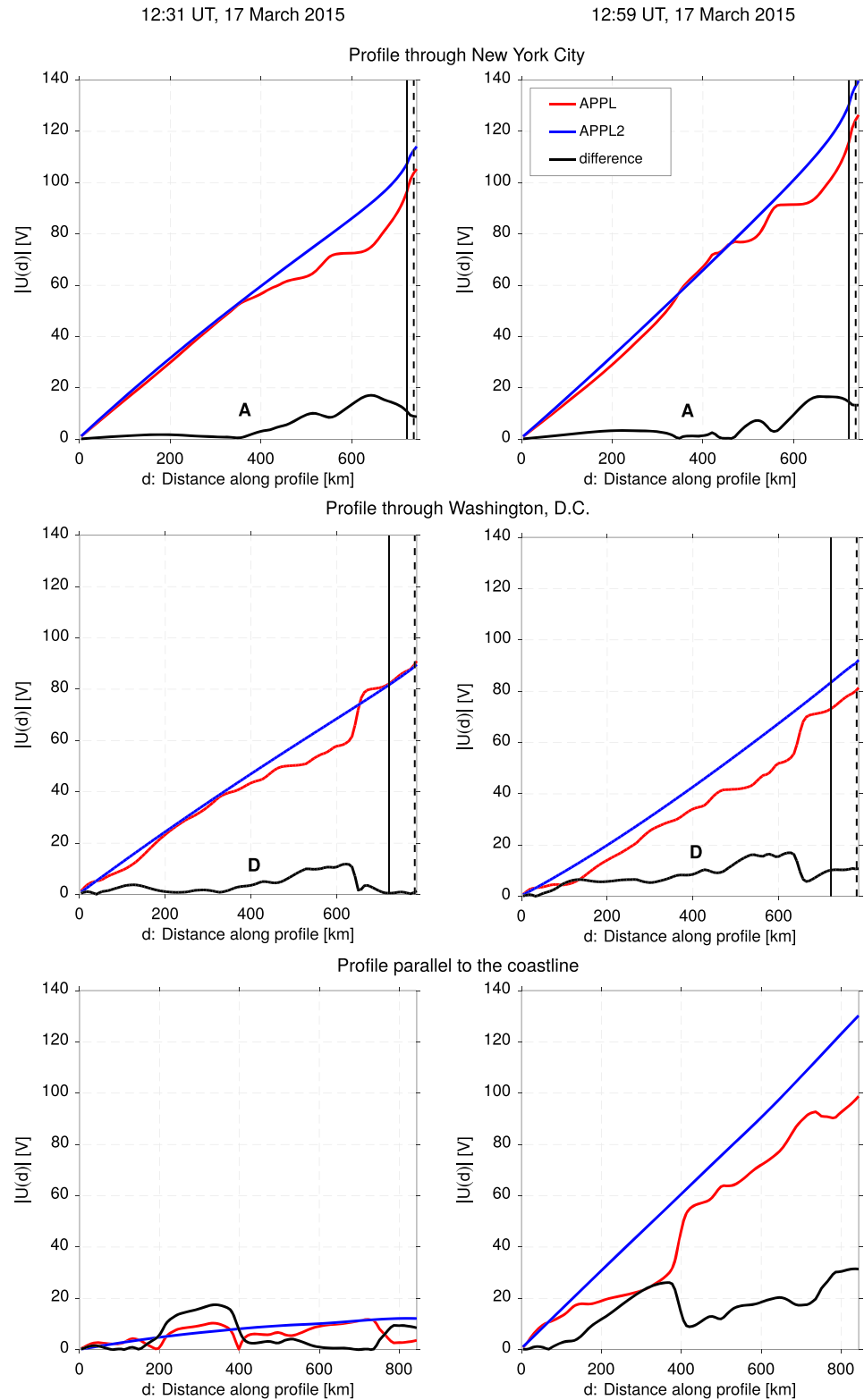
Figure 12. Absolute values of voltages (integrated GEF), |*U*|, along three profiles calculated in the APPL and APPL2 (with laterally homogeneous landmass conductivity) models, and their absolute differences. The results are presented as a function of interval of integration, *d*, at 12:31 UT (left) and 12:59 UT (right), 17 March 2015. (top and middle) |*U*| along land parts of NYC and WDC profiles, respectively. (bottom) |*U*| along the coastal profile. Solid vertical black lines mark the centers of the cities. Dashed vertical black lines mark the coasts. A and D are land parts of NYC and WDC profiles, respectively. Note different scales in all plots.

storm whereas Love et al. (2019) performed their analysis for multiple geomagnetic storms that occurred in 1983–2016, including stronger geomagnetic storms in March 1989 and October 2003. Our modeling results also significantly differ from the results of Love et al. (2019) for the northern MT sites that were not used for the APPL model construction.

3.3. Modeling Voltages

It is well known that computation of spatiotemporal evolution of the GEF is only a prerequisite for quantitative assessment of space weather hazard to technological systems. Ultimately, one has to calculate GICs flowing in these systems. Such calculations are based on the knowledge of the topology of transmission lines, their design parameters and voltages induced in the lines. The latter are calculated as integrals of the GEF along these lines. Note that a rule of thumb is that the longer the lines the larger GICs. In GIC research it is often assumed that effects arising from small-scale conductivity inhomogeneities are unimportant, because the integration of the GEF leads to smoothing of these effects (at least for long enough lines) or, in the best scenarios, to their elimination (Thomson et al., 2005; Viljanen et al., 2012). To question this statement, we integrated the GEF obtained in the APPL model and in the APPL2 model along NYC, WDC, and coastal profiles (recall that these profiles were chosen to imitate transmission lines; obviously, in the case of NYC and WDC profiles, only their land parts are relevant for voltage calculations).

Absolute values of integrals of the GEF along the profiles, or, in other words, absolute values of voltages, $|U|$, versus distance along profiles, d (or, in other words, versus interval of integration), are shown in Figure 12. It is seen that the difference between results for the APPL and APPL2 models varies with respect to profile and time instant and generally is not smoothed out with the increase of interval of integration; this clearly illustrates the fact that 3-D conductivity inhomogeneities can significantly affect the voltage. Figure 13 puts more weight on this inference. The left column in this figure demonstrates time series of $|U|$ along profiles for two considered models. One can notice that, for many time instants and all profiles, $|U|$ calculated in the APPL2 model exceed those for the APPL model. Results in the right column of the figure show the difference between the APPL and APPL2 $|U|$ in a more quantitative way. What is demonstrated here is the absolute differences between $|U|$ calculated in two models versus the APPL $|U|$. In addition, lines in the figure distinguish different (from 10% to 50%) relative differences between the APPL and APPL2 results. For example, for all (red) circles lying above 10% line the difference between modeling results is larger than 10%. There is a clear trend in the results: larger differences occur for smaller values of $|U|$. In contrast, for time instants with maximum amplification of the GEF (peak moments of the geomagnetic storm, which are considered to be the most hazardous) the absolute difference diminishes. However, there are time instants with both large values of $|U|$ (> 60 V) and rather large (> 20%) relative differences. The profile parallel to the coastline is affected by the presence of 3-D landmass inhomogeneities especially strongly. In some cases of large values of the $|U|$ (> 60 V) relative differences between modeling results for the APPL and APPL2 exceed 40%. From this model study we can conclude that effects originating from 3-D conductivity inhomogeneities are not fully eliminated during the integration of the GEF. Obviously, the strength of these effects depends on the actual geometry of the transmission networks which is far more complex than that considered in this paper.

Nevertheless, our results agree with results of Lucas et al. (2018), who calculated voltages across actual power transmission lines in the mid-Atlantic region of the United States. They convolve experimental MT impedances (both regional 1-D scalar impedances and 3-D tensor impedances estimated from EarthScope MT data) to calculate the GEF and then compute voltages from the GEF. Their results show that the use of 3-D impedances (which allows to take effects from 3-D landmass inhomogeneities into consideration) produces substantially more spatially variable GEF than this calculated utilizing regional 1-D impedances and that the integration of the GEF along power transmission lines does not necessarily smooth out the variability of the GEF.

3.4. Spatially Nonuniform Versus Plane Wave Source

All results presented in previous sections are obtained using a laterally varying (MHD) source. One can argue that this is an unnecessary complication, since the considered region (eastern United States) mostly lies in midlatitudes and the plane wave approach (Campanya et al., 2019; Kelbert et al., 2017; Lucas et al., 2018; Love et al., 2019; Torta et al., 2017) is sufficient to reproduce the GEF in the region. In this section we explore whether this is indeed the case by comparing the GEF calculated using the MHD source and the GEF obtained using a plane wave concept. The plane wave results are obtained as follows.
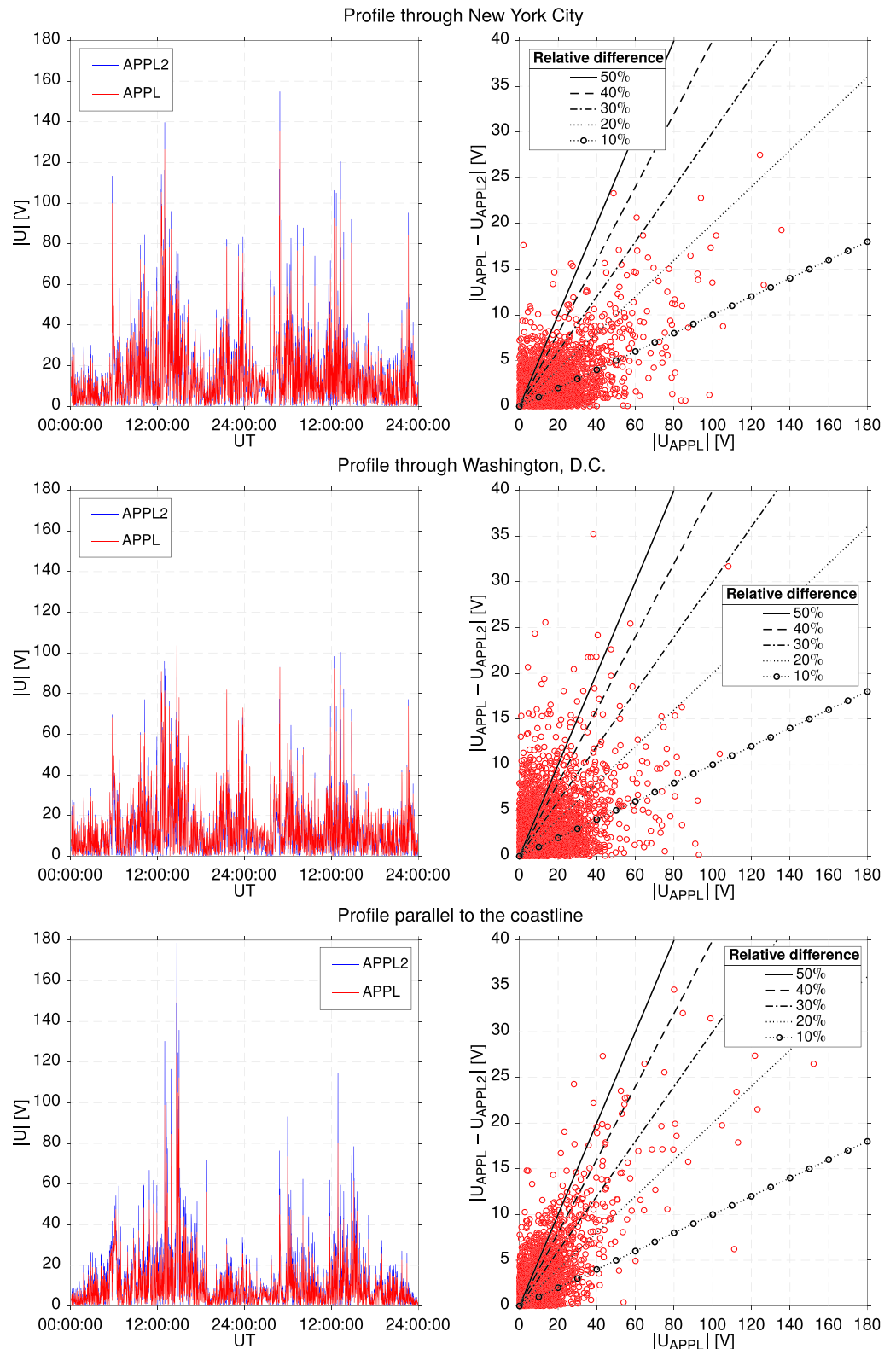
Figure 13. (left) Time series of $|U|$ along three profiles calculated in the APPL and APPL2 (with laterally homogeneous landmass conductivity) models. (right) absolute differences between U calculated in the APPL and APPL2 models versus $|U|$ calculated in the APPL model. Lines marking relative differences (from 10% to 50%) between the APPL and APPL2 modeling results are also demonstrated; for instance, for all the circles lying above 10% line the difference between modeling results is larger than 10%.
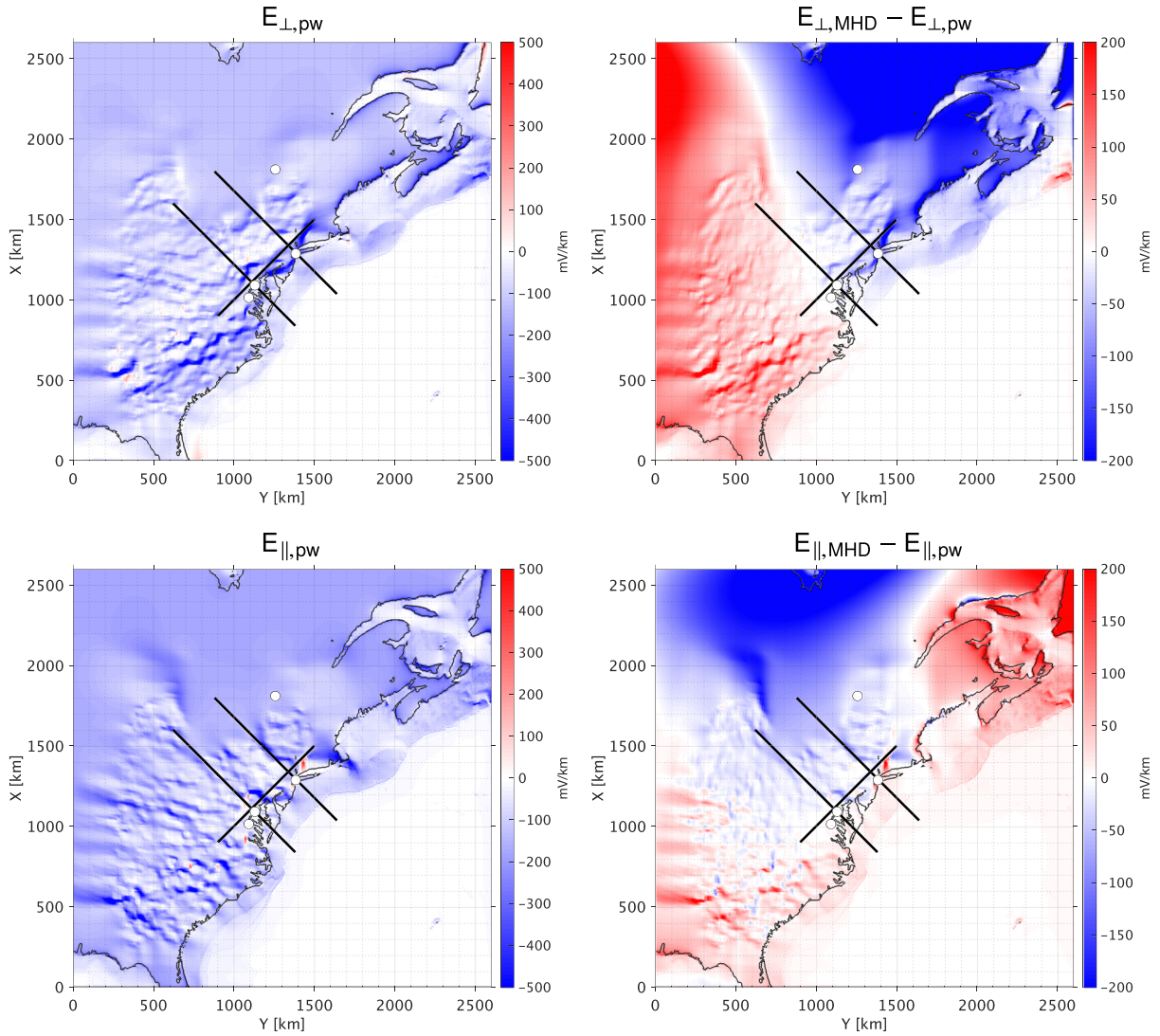
Figure 14. (left) Snapshots of the GEF components perpendicular (top) and parallel (bottom) to the coastline calculated in the APPL model using plane wave approach. (right) The difference between results calculated using laterally nonuniform (MHD) source and plane wave approach. The results are shown at 12:59 UT on 17 March 2015. Note different color scales in left and right plots.

1. 3-D EM forward modeling is carried out by *extrEMe* code (Kruglyakov et al., 2016) with two (laterally uniform) plane wave sources at FFT frequencies corresponding to periods from 2 min to 48 hr. Calculations are performed using the APPL 3-D conductivity model. 3-D MT intersite impedances $Z^i(\mathbf{r}_s, \mathbf{r}_b, \omega)$ (Campanya et al., 2019; Hermance & Thayer, 1975; Kruglyakov & Kuvshinov, 2019) that relate the surface horizontal electric field at each grid point $\mathbf{r}_s$ with the surface horizontal magnetic field at a fixed base site $\mathbf{r}_b$

$$\mathbf{E}_h(\mathbf{r}_s, \omega) = \frac{1}{\mu_0} Z^i(\mathbf{r}_s, \mathbf{r}_b, \omega) \mathbf{B}_h(\mathbf{r}_b, \omega), \quad Z^i(\mathbf{r}_s, \mathbf{r}_b, \omega) = \begin{pmatrix} Z^i_{xx} & Z^i_{xy} \\ Z^i_{yx} & Z^i_{yy} \end{pmatrix},$$ (7)

   are then calculated for each FFT frequency ω. In this model study $\mathbf{r}_b$ coincides with location of FRD observatory.

2. Time-varying horizontal magnetic field at the location of the FRD which was calculated earlier via 3-D EM forward modeling using the MHD source and the APPL model is Fourier transformed to obtain $\mathbf{B}_h^{MHD}(\mathbf{r}_{FRD}, \omega)$. This field is considered as a "true" magnetic field, thus mimicking the actual magnetic field measured at FRD observatory.
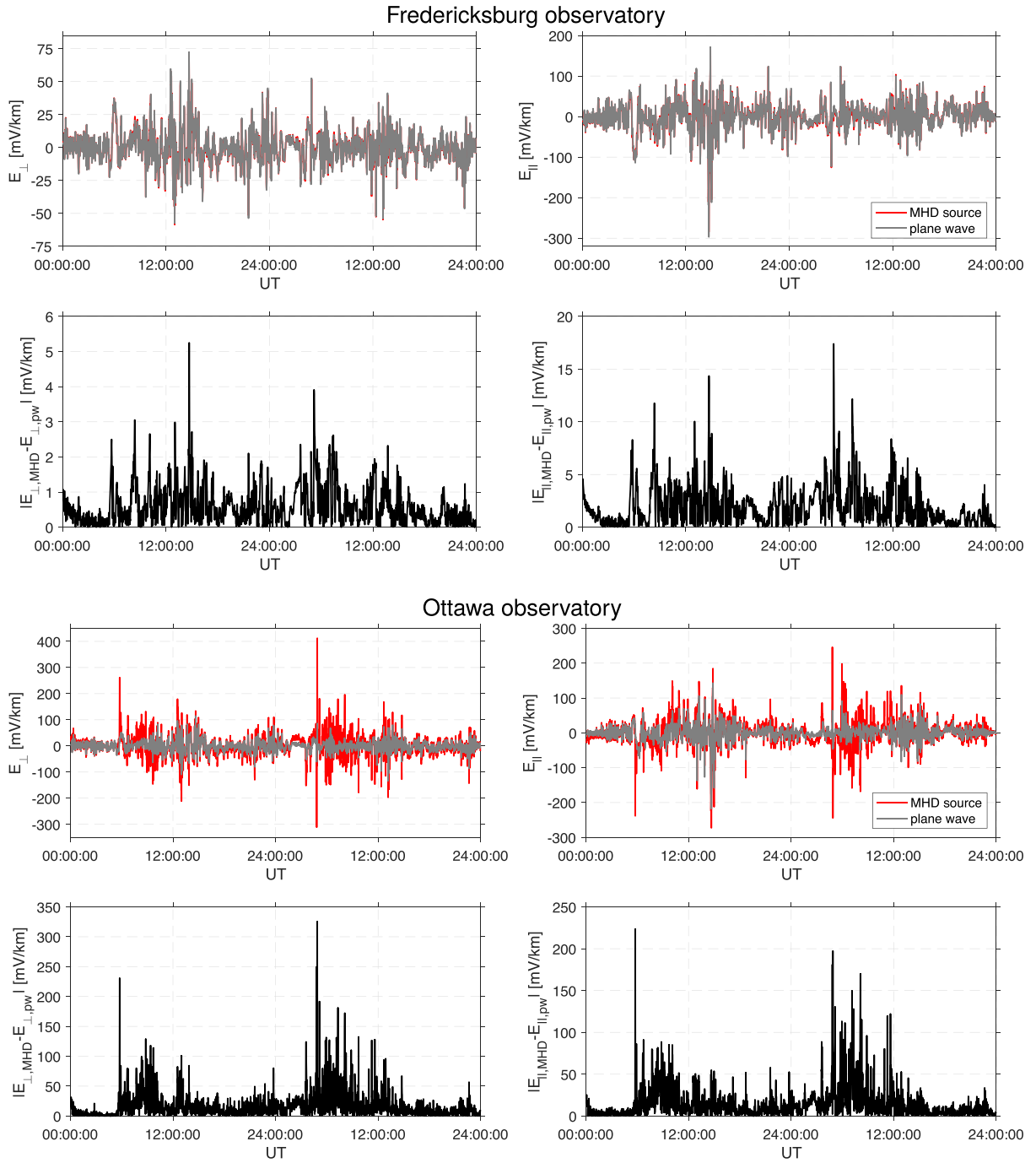
Fredericksburg observatory

Ottawa observatory

Figure 15. Time series of the GEF at FRD and OTT observatories' locations calculated using laterally nonuniform (MHD) source and plane wave approach. Modelings were carried out for the APPL model. Results are demonstrated for GEF components perpendicular and parallel to the coast. Absolute differences between results are also shown (the second and the fourth rows).

3. The (horizontal) GEF is calculated for each frequency and each grid point as

$$\mathbf{E}_h^{pw}(\mathbf{r}_s, \omega) = \frac{1}{\mu_0} Z^i(\mathbf{r}_s, \mathbf{r}_{FRD}, \omega) \mathbf{B}_h^{MHD}(\mathbf{r}_{FRD}, \omega). \qquad (8)$$

4. Finally, an inverse FFT is performed for the frequency domain GEF to obtain the "plane wave" GEF in the time domain.
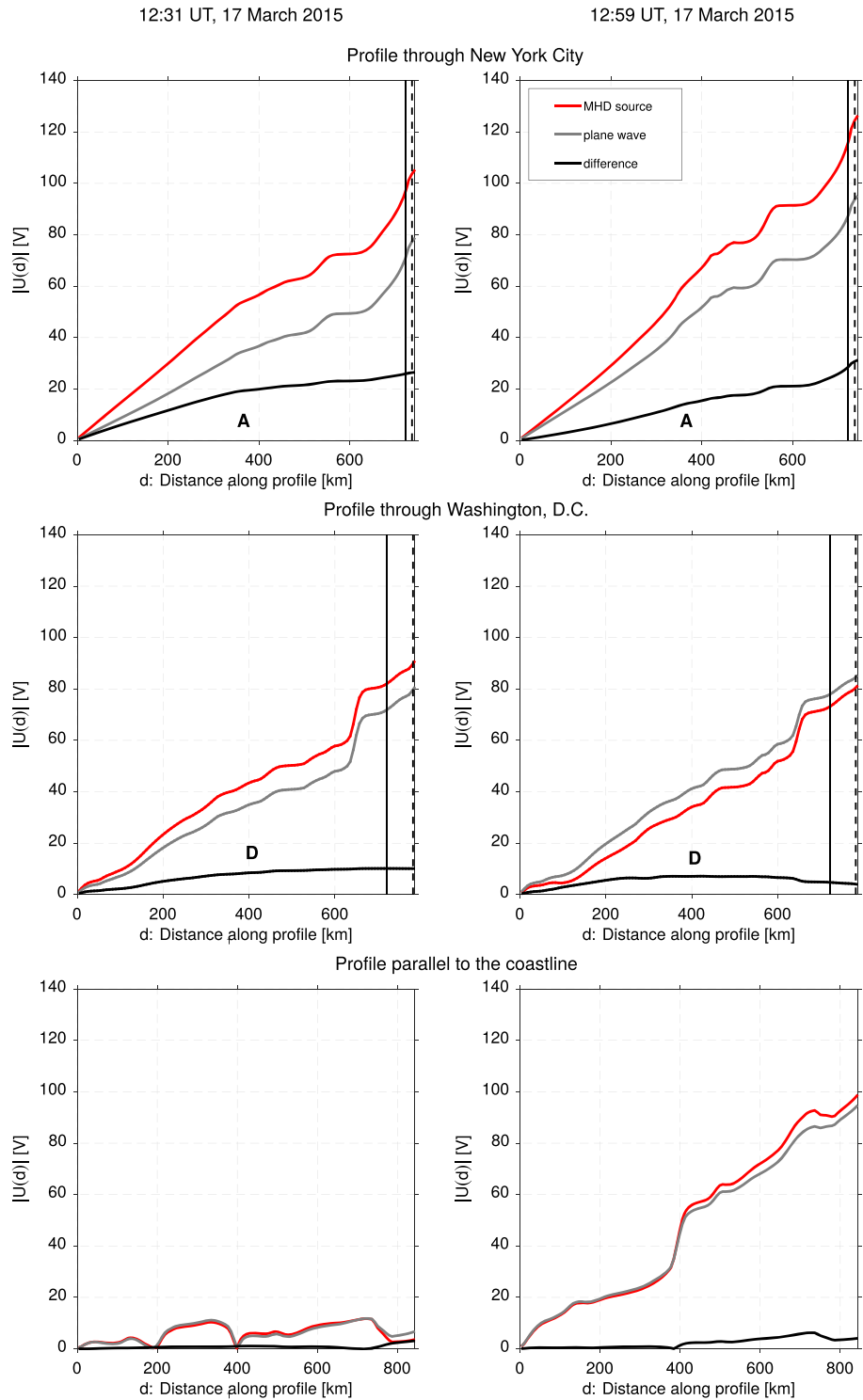
Figure 16. Absolute values of voltages (integrated GEF), |U|, along three profiles calculated using laterally nonuniform (MHD) source and plane wave approach, and their absolute differences. The results are presented as a function of interval of integration, d, at 12:31 UT (left) and 12:59 UT (right), 17 March 2015. Modelings were carried out for the APPL model. (top and middle) |U| along land parts of NYC and WDC profiles, respectively. (bottom) |U| along the coastal profile. Solid vertical black lines mark the centers of the cities. Dashed vertical black lines mark the coasts. A and D are land parts of NYC and WDC profiles, respectively. Note different scales in all plots.

The left plots in Figure 14 show the spatial distribution of the GEF at 12:59 UT calculated using plane wave approach described above, whereas the right plots present the difference between results calculated using the MHD source and plane wave results. Interestingly, the difference between results is large not only in the northern part of the model, where the source reveals large spatial gradients (see Figure 5), but also in the southern part, especially in the regions with large lateral contrasts of conductivity. Figure S7 in the supporting information shows in a similar manner the results at 12:31 UT.

Figure 15 demonstrates the comparison of the GEF time series at locations of two observatories, FRD and OTT (see Figure 1), calculated using the MHD and plane wave sources. It is seen that for FRD observatory location modeling results differ insignificantly. The difference between modeling results for OTT observatory is expectedly large due to effects from noticeable lateral (see, again, Figure 5) variability of the MHD source.

Similar results were reported by Love et al. (2019), who studied the GEF behavior in the northeastern United States using measured MT impedance tensors. They noted that in this region it would be difficult to map GEF variations over the course of an individual magnetic storm using geomagnetic field data from sparsely distributed observatories and exploiting a plane wave approach, since storm time signals are most probably not fully consistent with the plane wave approximation.

We also look at voltages generated by plane wave GEF. Figure 16 is the analog of Figure 12 demonstrating $|U|$ along three profiles at two time instants. $|U|$ along the profile parallel to the coastline is not strongly affected by the change of the source, at least for the selected time instants. The difference between modeling results for two aforementioned sources is especially large for NYC profile due to its more northern location.

Figure 17 is similar to Figure 13. Left plots demonstrate time series of $|U|$ along NYC, WDC and coastal profiles for two aforementioned sources. One can see that $|U|$ along NYC profile is strongly affected by the change of the source. For many time instants, the voltages calculated with spatially nonuniform source are much larger than the voltages calculated with plane wave source. The right plots in Figure 17 show the absolute differences between U calculated with the MHD and plane wave sources versus $|U|$ calculated with MHD source. As it was previously noted, the change of the source dramatically affects $|U|$ along NYC profile. The absolute difference between voltages reaches almost 60 V. For many time instants with large $|U|$, the relative difference between modeling results is larger than 20%. For WDC profile the difference between $|U|$ is still quite large (maximum absolute difference exceeds 50 V) but smaller than in the case of NYC profile, which is also expressed in smaller values of the relative differences. $|U|$ along profile parallel to the coastline is not affected by the change of the source as strongly as $|U|$ along NYC and WDC profiles. The absolute difference does not exceed 25 V; the relative difference for time instants of peak amplification of the GEF usually does not exceed 10%.

4. Conclusions

In this work we used a 3-D EM forward modeling framework, as described in Ivannikova et al. (2018), to explore the GEF behavior in the eastern United States during the St. Patrick's Day geomagnetic storm in March 2015. The source that induces a conducting earth during this event was retrieved from a dedicated MHD simulation. By exploiting MHD models, one has an opportunity to specify both large-scale (midlatitude) and small-scale (high-latitude) inducing sources.

First we explored the coastal effect using a 3-D model with laterally uniform landmass conductivity. According to modeling results, and as expected, the coastal effect can penetrate deep (several hundred kilometers) on land. The magnitudes of the GEF obtained using 3-D modeling can exceed the results of 1-D modeling by about a factor of 2–3 in the coastal areas. The severity of the coastal effect strongly depends on the choice of the (homogeneous) landmass conductivity; the smaller the landmass conductivity the stronger the effect. We analyzed the GEF behavior along a few profiles that mimic transmission lines in the region and found that the lines perpendicular to the coast are more affected by the coastal effect than those parallel to the coast.

The incorporation of realistic landmass 3-D conductivity heterogeneities into the model dramatically influences the GEF behavior on land. Effects originating from these heterogeneities appear to be comparable in magnitude to the coastal effect. These effects can also significantly influence the values of the integrated GEF (voltages). This result is of special importance since computation of GICs relies on voltages, but not
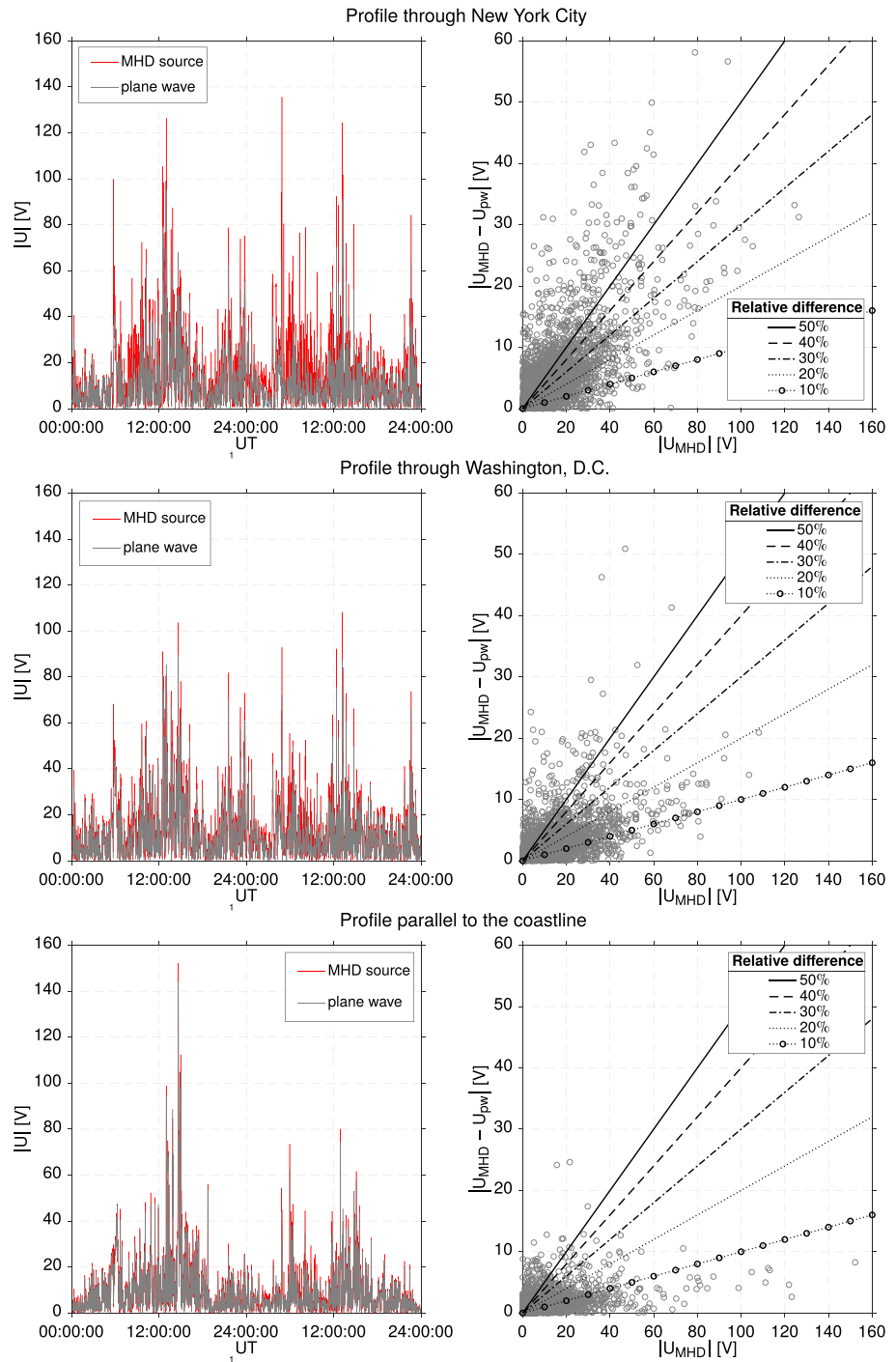
Figure 17. (left) Time series of |U| along three profiles calculated using laterally nonuniform (MHD) source and plane wave approach. (right) absolute differences between U calculated using two aforementioned sources versus |U| calculated using the MHD source. Modelings were carried out for the APPL model. Lines marking relative differences (from 10% to 50%) between U calculated using two aforementioned sources are also demonstrated; for instance, for all the circles lying above 10% line the difference between modeling results is larger than 10%.

on GEFs themselves. It emphasizes the necessity of realistic 3-D regional conductivity models usage for rigorous geoelectric hazard assessment.

We also compare the GEF and voltages induced by a laterally varying (MHD) source to those calculated using a plane wave method and show that the difference is noticeable even in middle latitudes that are commonly considered to be negligibly affected by lateral nonuniformity of the source. Overall, the differences in GEFs and integrated GEFs increase toward the north of the model where, as expected, the effects from high-latitude (laterally variable) external currents become significant.

A final remark concerns the comparison of modeling results to observations. Such comparison is omitted in the main text of the paper and is available as supporting information (Figures S8 and S9 for FRD and OTT observatories, respectively; comparison is limited to magnetic field only, since there were no electric field measurements at FRD and OTT). The fit of the modeling results and observations is encouraging, in terms of both amplitudes and long-period variations. However, so far it is most likely not possible to reproduce the exact EM field variations using the MHD modeling. At the same time the use of the MHD modeling allows to simulate long-period trends in the observations with a certain level of accuracy. Recently this was also demonstrated by Liemohn et al. (2018), who were able to reliably reproduce the Dst index dynamics during the 27-month time interval using the SWMF. Apparently the MHD modeling provides an adequate physics-based source for simulation of ground-based EM field variations, which is especially important for regions with no or few geomagnetic observatories.

References

Alekseev, D., Kuvshinov, A., & Palshin, N. (2015). Compilation of 3D global conductivity model of the Earth for space weather applications. *Earth, Planets and Space*, *67*, 108. https://doi.org/10.1186/s40623-015-0272-5

Amante, C., & Eakins, B. W. (2009). ETOPO1 1 arc-minute global relief model: Procedures, data sources and analysis. NOAA Technical Memorandum NESDIS NGDC-24. National Geophysical Data Center, NOAA, *10*, V5C8276M. https://doi.org/10.7289/V5C8276M

Bailey, R. L., Halbedl, T. S., Schattauer, I., Achleitner, G., & Leonhardt, R. (2018). Validating GIC models with measurements in Austria: Evaluation of accuracy and sensitivity to input parameters. *Space Weather*, *16*, 887–902. https://doi.org/10.1029/2018SW001842

Bailey, R. L., Halbedl, T. S., Schattauer, I., Römer, A., Achleitner, G., Beggan, C. D., et al. (2017). Modelling geomagnetically induced currents in midlatitude Central Europe using a thin-sheet approach. *Annales de Geophysique*, *35*(3), 751–761. https://doi.org/10.5194/angeo-35-751-2017

Beggan, C. D., Beamish, D., Richards, A., Kelly, G. S., & Thomson, A. W. P. (2013). Prediction of extreme geomagnetically induced currents in the UK high-voltage network. *Space Weather*, *11*, 407–419. https://doi.org/10.1002/swe.20065

Belakhovsky, V., Pilipenko, V., Engebretson, M., Sakharov, Y., & Selivanov, V. (2019). Impulsive disturbances of the geomagnetic field as a cause of induced currents of electric power lines. *Journal of Space Weather and Space Climate*, *9*, A18. https://doi.org/10.1051/swsc/2019015

Campanya, J., Gallagher, P. T., Blake, S. P., Gibbs, M., Jackson, D., Beggan, C. D., et al. (2019). Modelling geoelectric fields in Ireland and the UK for space weather applications. *Space Weather*, *17*, 216–237. https://doi.org/10.1029/2018SW001999

Chave, A. D., & Jones, A. G. (2012). *Introduction to the magnetotelluric method. In the magnetotelluric method: Theory and practice.* Cambridge: Cambridge University Press. https://doi.org/10.1017/CBO9781139020138

De Zeeuw, D. L., Sazykin, S., Wolf, R. A., Gombosi, T. I., Ridley, A. J., & Toth, G. (2004). Coupling of a global MHD code and an inner magnetospheric model: Initial results. *Journal of Geophysical Research*, *109*, A12219. https://doi.org/10.1029/2003JA010366

Dimmock, A. P., Rosenqvist, L., Hall, J.-O., Viljanen, A., Yordanova, E., Honkonen, I., et al. (2019). The GIC and geomagnetic response over Fennoscandia to the 7–8 September 2017 geomagnetic storm. *Space Weather*, *17*, 989–1010. https://doi.org/10.1029/2018SW002132

Divett, T., Ingham, M., Beggan, C. D., Richardson, G. S., Rodger, C. J., Thomson, A. W. P., & Dalzell, M. (2017). Modeling geoelectric fields and geomagnetically induced currents around New Zealand to explore GIC in the South Island's electrical transmission network. *Space Weather*, *15*, 1396–1412. https://doi.org/10.1002/2017SW001697

Fischer, G. (1979). Electromagnetic induction effects at an ocean coast. *Proceedings of the IEEE*, *67*(7), 1044–1050. https://doi.org/10.1109/PROC.1979.11387

Fischer, G., & Weaver, J. T. (1986). Theoretical investigation of the ocean-coast effect at a passive continental margin. *Physics of the Earth and Planetary Interiors*, *42*(4), 246–254. https://doi.org/10.1016/0031-9201(86)90027-0

Gannon, J. L., Birchfield, A. B., Shetye, K. S., & Overbye, T. J. (2017). A comparison of peak electric fields and GICs in the Pacific Northwest using 1-D and 3-D conductivity. *Space Weather*, *15*, 1535–1547. https://doi.org/10.1002/2017SW001677

Gilbert, J. L. (2005). Modeling the effect of the ocean-land interface on induced electric fields during geomagnetic storms. *Space Weather*, *3*, S04A03. https://doi.org/10.1029/2004SW000120

Grayver, A. V., Munch, F. D., Kuvshinov, A. V., Khan, A., Sabaka, T. J., & Tøffner-Clausen, L. (2017). Joint inversion of satellite-detected tidal and magnetospheric signals constrains electrical conductivity and water content of the upper mantle and transition zone. *Geophysical Research Letters*, *44*, 6074–6081. https://doi.org/10.1002/2017GL073446

Hermance, J. F., & Thayer, R. E (1975). The telluric-magnetotelluric method. *Geophysics*, *40*(4), 664–668. https://doi.org/10.1190/1.1440557

Honkonen, I., Kuvshinov, A., Rastätter, L., & Pulkkinen, A. (2018). Predicting global ground geoelectric field with coupled geospace and three-dimensional geomagnetic induction models. *Space Weather*, *16*, 1028–1041. https://doi.org/10.1029/2018SW001859

Ivannikova, E., Kruglyakov, M., Kuvshinov, A., Rastätter, L., & Pulkkinen, A. (2018). Regional 3-D modeling of ground electromagnetic field due to realistic geomagnetic disturbances. *Space Weather*, *16*, 476–500. https://doi.org/10.1002/2017SW001793

Jiracek, G. R. (1990). Near-surface and topographic distortions in electromagnetic induction. *Surveys in Geophysics*, *11*(2–3), 163–203. https://doi.org/10.1007/BF01901659

Kelbert, A., Balch, C. C., Pulkkinen, A., Egbert, G. D., Love, J. J., Rigler, E. J., & Fujii, I. (2017). Methodology for time-domain estimation of storm time geoelectric fields using the 3-D magnetotelluric response tensors. *Space Weather*, *15*, 874–894. https://doi.org/10.1002/2017SW001594

Kelbert, A., Bedrosian, P., & Murphy, B. S. (2019). The first 3D conductivity model of the contiguous United States. In J. L. Gannon, A. Swidinsky, & Z. Xu (Eds.), *Geomagnetically induced currents from the Sun to the power grid*, Geophysical Monograph Series (pp. 127–151). Washington, DC: John Wiley Inc. https://doi.org/10.1002/9781119434412.ch8

Kelbert, A., Egbert, G. D., & Schultz, A. (2011). IRIS DMC data services products. The magnetotelluric transfer functions. https://doi.org/10.17611/DP/EMTF.1

Kelbert, A., Meqbel, N., Egbert, G. D., & Tandon, K. (2014). Mod EM: A modular system for inversion of electromagnetic geophysical data. *Computational Geosciences*, *66*, 40–53. https://doi.org/10.1016/j.cageo.2014.01.010

Kruglyakov, M., Geraskin, A., & Kuvshinov, A. (2016). Novel accurate and scalable 3-D MT forward solver based on a contracting integral equation method. *Computers & Geosciences*, *96*, 208–217. https://doi.org/10.1016/j.cageo.2016.08.017

Kruglyakov, M., & Kuvshinov, A. (2019). 3-D inversion of MT impedances and inter-site tensors, individually and jointly. New lessons learnt. *Earth Planets Space*, *71*, 4. https://doi.org/10.1186/s40623-018-0972-8

Kuvshinov, A. (2008). 3-D global induction in the oceans and solid earth: Recent progress in modeling magnetic and electric fields from sources of magnetospheric, ionospheric and oceanic origin. *Surveys in Geophysics*, *29*(2), 139–186. https://doi.org/10.1007/s10712-008-9045-z

Kuvshinov, A., Avdeev, D., & Pankratov, O. (1999). Global induction by Sq and Dst sources in the presence of oceans: Bimodal solutions for non-uniform spherical surface shells above radially symmetric earth models in comparison to observations. *Geophysical Journal International*, *137*(3), 630–650. https://doi.org/10.1046/j.1365-246x.1999.00827.x

Liemohn, M., Ganushkina, N. Y., De Zeeuw, D. L., Rastätter, L., Kuznetsova, M., Welling, D. T., et al. (2018). Real-time SWMF at CCMC: Assessing the Dst output from continuous operational simulations. *Space Weather*, *16*, 1583–1603. https://doi.org/10.1029/2018SW001953

Liu, C., Wang, X., Wang, H., & Zhao, H. (2018). Quantitative influence of coast effect on geomagnetically induced currents in power grids: A case study. *Journal of Space Weather and Space Climate*, *8*, A60. https://doi.org/10.1051/swsc/2018046

Love, J. J., Lucas, G., Bedrosian, P. A., & Kelbert, A. (2019). Extreme-value geoelectric amplitude and polarization across the northeast United States. *Space Weather*, *17*, 379–395. https://doi.org/10.1029/2018sw002068

Love, J. J., Lucas, G. M., Kelbert, A., & Bedrosian, P. A. (2018a). Geoelectric hazard maps for the Mid-Atlantic United States: 100 year extreme values and the 1989 magnetic storm. *Geophysical Research Letters*, *44*, 5–14. https://doi.org/10.1002/2017GL076042

Love, J. J., Lucas, G. M., Kelbert, A., & Bedrosian, P. A. (2018b). Geoelectric hazard maps for the Pacific Northwest. *Space Weather*, *16*, 1114–1127. https://doi.org/10.1029/2018SW001844

Lucas, G. M., Love, J. J., & Kelbert, A. (2018). Calculation of voltages in electric power transmission lines during historic geomagnetic storms: An investigation using realistic Earth impedances. *Space Weather*, *16*, 181–195. https://doi.org/10.1002/2017SW001779

Marshall, R. A., Wang, L., Paskos, G. A., Olivares-Pulido, G., Van Der Walt, T., Ong, C., et al. (2019). Modeling geomagnetically induced currents in Australian power networks using different conductivity models. *Space Weather*, *17*, 727–756. https://doi.org/10.1002/2017SW001793

Murphy, B. S., & Egbert, G. D. (2017). Electrical conductivity structure of southeastern North America: Implications for lithospheric architecture and Appalachian topographic rejuvenation. *Earth and Planetary Science Letters*, *462*, 66–75. https://doi.org/10.1016/j.epsl.2017.01.009

Nakamura, S., Ebihara, Y., Fujita, S., Goto, T., Yamada, N., Watari, S., & Omura, Y. (2018). Time domain simulation of geomagnetically induced current (GIC) flowing in 500-kV power grid in Japan including a three-dimensional ground inhomogeneity. *Space Weather*, *16*, 1946–1959. https://doi.org/10.1029/2018SW002004

Pankratov, O., Avdeyev, D., & Kuvshinov, A. (1995). Electromagnetic field scattering in a heterogeneous Earth: A solution to the forward problem. *Izvestiya, Physics of the Solid Earth*, *31*(3), 201–209.

Parkinson, W. D., & Jones, F. W. (1979). The geomagnetic coast effect. *Reviews of Geophysics*, *17*(8), 1999–2015. https://doi.org/10.1029/RG017i008p01999

Pokhrel, S., Nguyen, B., Rodriguez, M., Bernabeu, E., & Simpson, J. J. (2018). A finite difference time domain investigation of electric field enhancements along ocean-continent boundaries during space weather events. *Journal of Geophysical Research: Space Physics*, *123*, 5033–5046. https://doi.org/10.1029/2017JA024648

Powell, K. G., Roe, P. L., Linde, T. J., Gombosi, T. I., & De Zeeuw, D. L. (1999). A solution-adaptive upwind scheme for ideal magnetohydrodynamics. *Journal of Computational Physics*, *154*(2), 284–309. https://doi.org/10.1006/jcph.1999.6299

Püthe, C., & Kuvshinov, A. (2013). Towards quantitative assessment of the hazard from space weather. Global 3-D modellings of the electric field induced by a realistic geomagnetic storm. *Earth, Planets and Space*, *65*, 1017–1025. https://doi.org/10.5047/eps.2013.03.003

Püthe, C., Kuvshinov, A., Khan, A., & Olsen, N. (2015). A new model of Earth's radial conductivity structure derived from over 10 yr of satellite and observatory magnetic data. *Geophysical Journal International*, *203*(3), 1864–1872. https://doi.org/10.1093/gji/ggv407

Püthe, C., Manoj, N., & Kuvshinov, A. (2014). Reproducing electric field observations during magnetic storms by means of rigorous 3-D modelling and distortion matrix co-estimation. *Earth, Planets and Space*, *66*, 162–171. https://doi.org/10.1186/s40623-014-0162-2

Rastätter, L., Toth, G., Kuznetsova, M. M., & Pulkkinen, A. A. (2014). CalcDeltaB: An efficient post processing tool to calculate ground-level magnetic perturbations from global magnetosphere simulations. *Space Weather*, *12*, 553–565. https://doi.org/10.1002/2014SW001083

Ridley, A. J., Gombosi, T. I., & De Zeeuw, D. L. (2004). Ionospheric control of the magnetosphere: Conductance. *Annales de Geophysique*, *22*, 567–584. https://doi.org/10.5194/angeo-22-567-2004

Rosenqvist, L., & Hall, J. (2019). Regional 3-D modeling and verification of geomagnetically induced currents in Sweden. *Space Weather*, *17*, 27–36. https://doi.org/10.1029/2018SW002084

Thomson, A. W. P., McKay, A. J., Clarke, E., & Reay, S. J. (2005). Surface electric fields and geomagnetically induced currents in the Scottish power grid during the 30 October 2003 geomagnetic storm. *Space Weather*, *3*, S11002. https://doi.org/10.1029/2005SW000156

Torta, J. M., Marcuello, A., Campanya, J., Marsal, S., Queralt, P., & Ledo, J. (2017). Improving the modeling of geomagnetically induced currents in Spain. *Space Weather*, *15*, 691–703. https://doi.org/10.1002/2017SW001628

Toth, G., Sokolov, I. V., Gombosi, T. I., Chesney, D. R., Clauer, C. R., De Zeeuw, D. L., et al. (2005). Space Weather Modeling Framework: A new tool for the space science community. *Journal of Geophysical Research*, *110*, A12226. https://doi.org/10.1029/2005JA011126

Toth, G., van der Holst, B., Sokolov, I., De Zeeuw, D. L., Gombosi, T., Fang, F., et al. (2012). Adaptive numerical algorithms in space weather modeling. *Journal of Computational Physics*, *231*(3), 870–903. https://doi.org/10.1016/j.jcp.2011.02.006

Viljanen, A., Pirjola, R., Wik, M., Adam, A., Pracser, E., Sakharov, Y., & Katkalov, J. (2012). Continental scale modelling of geomagnetically induced currents. *Journal of Space Weather and Space Climate*, *2*, A17. https://doi.org/10.1051/swsc/2012017

Wang, L., Lewis, A. M., Ogawa, Y., Jones, W. V., & Costelloe, M. T. (2016). Modeling geomagnetic induction hazards using a 3-D electrical conductivity model of Australia. *Space Weather*, *14*, 1125–1135. https://doi.org/10.1002/2016SW001436

Weaver, J. T. (1963). The electromagnetic field within a discontinuous conductor with reference to geomagnetic micropulsations near a coastline. *Canadian Journal of Physics*, *41*(3), 484–495. https://doi.org/10.1139/p63-051

Weaver, J. T., & Dawson, T. W. (1992). Adjustment distance in TM mode electromagnetic induction. *Geophysical Journal International*, *108*(1), 293–300. https://doi.org/10.1111/j.1365-246X.1992.tb00858.x

Erratum

This paper has been corrected from the initially published version to correct a misspelling in Lutz Rastatter's name, and to correct the DOI of Bailey et al 2017. This corrected version may be considered the version of record.